The Astrophysical Journal, 777:43 (21pp), 2013 November 1 doi:10.1088/0004-637X/777/1/43
© 2013. The American Astronomical Society. All rights reserved. Printed in the U.S.A.

CLASH: COMPLETE LENSING ANALYSIS OF THE LARGEST COSMIC LENS MACS J0717.5+3745 AND SURROUNDING STRUCTURES*

Elinor Medezinski[1], Keiichi Umetsu[2], Mario Nonino[3], Julian Merten[4], Adi Zitrin[5], Tom Broadhurst[6,7], Megan Donahue[8], Jack Sayers[9], Jean-Claude Waizmann[10], Anton Koekemoer[11], Dan Coe[11], Alberto Molino[12], Peter Melchior[13], Tony Mroczkowski[4,9,24], Nicole Czakon[9], Marc Postman[11], Massimo Meneghetti[10], Doron Lemze[1], Holland Ford[1], Claudio Grillo[14], Daniel Kelson[15], Larry Bradley[11], John Moustakas[16], Matthias Bartelmann[5], Narciso Benítez[12], Andrea Biviano[3], Rychard Bouwens[17], Sunil Golwala[9], Genevieve Graves[18], Leopoldo Infante[19], Yolanda Jiménez-Teja[6], Stephanie Jouvel[20], Ofer Lahav[21], Leonidas Moustakas[4], Sara Ogaz[11], Piero Rosati[22], Stella Seitz[23], and Wei Zheng[1]

[1] Department of Physics and Astronomy, The Johns Hopkins University, 3400 North Charles Street, Baltimore, MD 21218, USA; elinor@pha.jhu.edu
[2] Institute of Astronomy and Astrophysics, Academia Sinica, P.O. Box 23-141, Taipei 10617, Taiwan
[3] INAF/Osservatorio Astronomico di Trieste, via G.B. Tiepolo 11, I-34143 Trieste, Italy
[4] Jet Propulsion Laboratory, California Institute of Technology, MS 169-327, Pasadena, CA 91109, USA
[5] Institut für Theoretische Astrophysik, Universität Heidelberg, Zentrum für Astronomie, Philosophenweg 12, D-69120 Heidelberg, Germany
[6] Department of Theoretical Physics and History of Science, University of the Basque Country UPV/EHU, P.O. Box 644, E-48080 Bilbao, Spain
[7] Ikerbasque, Basque Foundation for Science, Alameda Urquijo, 36-5 Plaza Bizkaia, E-48011 Bilbao, Spain
[8] Department of Physics and Astronomy, Michigan State University, East Lansing, MI 48824, USA
[9] Division of Physics, Math, and Astronomy, California Institute of Technology, Pasadena, CA 91125, USA
[10] Dipartimento di Astronomia, Universit'a di Bologna, via Ranzani 1, I-40127 Bologna, Italy
[11] Space Telescope Science Institute, 3700 San Martin Drive, Baltimore, MD 21208, USA
[12] Instituto de Astrofísica de Andalucía (CSIC), E-18080 Granada, Spain
[13] Center for Cosmology and Astro-Particle Physics and Department of Physics, The Ohio State University, Columbus, OH 43210, USA
[14] Dark Cosmology Centre, Niels Bohr Institute, University of Copenhagen, Juliane Mariesvej 30, DK-2100 Copenhagen, Denmark
[15] Observatories of the Carnegie Institution of Washington, Pasadena, CA 91101, USA
[16] Department of Physics and Astronomy, Siena College, 515 Loudon Road, Loudonville, NY 12211, USA
[17] Leiden Observatory, Leiden University, 2300-RA Leiden, The Netherlands
[18] Department of Astronomy, University of California, 601 Campbell Hall, Berkeley, CA 94720, USA
[19] Centro de Astro-Ingeniería, Departamento de Astronomía y Astrofísica, Pontificia Universidad Católica de Chile, V. Mackenna 4860, Santiago, Chile
[20] Institut de Ciéncies de l'Espai (IEEC-CSIC), E-08193 Bellaterra (Barcelona), Spain
[21] Department of Physics and Astronomy, University College London, London WC1E 6BT, UK
[22] ESO-European Southern Observatory, D-85748 Garching bei München, Germany
[23] Universitäts-Sternwarte, München, Scheinerstr. 1, D-81679 München, Germany
Received 2013 April 3; accepted 2013 August 30; published 2013 October 15

ABSTRACT

The galaxy cluster MACS J0717.5+3745 ($z = 0.55$) is the largest known cosmic lens, with complex internal structures seen in deep X-ray, Sunyaev–Zel'dovich effect, and dynamical observations. We perform a combined weak- and strong-lensing analysis with wide-field $BVR_ci'z'$ Subaru/Suprime-Cam observations and 16-band *Hubble Space Telescope* observations taken as part of the Cluster Lensing And Supernova survey with Hubble. We find consistent weak distortion and magnification measurements of background galaxies and combine these signals to construct an optimally estimated radial mass profile of the cluster and its surrounding large-scale structure out to 5 Mpc h^{-1}. We find consistency between strong-lensing and weak-lensing in the region where these independent data overlap, <500 kpc h^{-1}. The two-dimensional weak-lensing map reveals a clear filamentary structure traced by distinct mass halos. We model the lensing shear field with nine halos, including the main cluster, corresponding to mass peaks detected above $2.5\sigma_\kappa$. The total mass of the cluster as determined by the different methods is $M_{\rm vir} \approx (2.8 \pm 0.4) \times 10^{15}\, M_\odot$. Although this is the most massive cluster known at $z > 0.5$, in terms of extreme value statistics, we conclude that the mass of MACS J0717.5+3745 by itself is not in serious tension with ΛCDM, representing only a $\sim 2\sigma$ departure above the maximum simulated halo mass at this redshift.

Key words: cosmology: observations – dark matter – galaxies: clusters: individual (MACS J0717.5+3745) – gravitational lensing: strong – gravitational lensing: weak

Online-only material: color figures

1. INTRODUCTION

In hierarchical structure formation theories, massive clusters are formed relatively recently and are still growing through the accretion of substructure. Accretion is predicted to occur preferentially along filaments with clusters at the nodes of intersection (Bond et al. 1996), a pattern which is now clearly visible in densely sampled large redshift surveys (Colless et al. 2001; Huchra et al. 2005), all-sky optical surveys such as the Sloan Digital Sky Survey (SDSS; Tegmark et al. 2004) and the Baryon Oscillation Spectroscopic Survey (BOSS; White et al. 2011), and large lensing shear surveys (e.g., Massey et al. 2007b; Van Waerbeke et al. 2013). Increasing numbers of clusters caught in the act of merging are found among the

* Based in part on data collected at the Subaru Telescope, which is operated by the National Astronomical Society of Japan.
[24] NASA Einstein Postdoctoral Fellow.

Table 1
Properties of the Galaxy Cluster MACSJ0717

Parameter	Value
ID	MACS J0717.5+3745
Optical position (J2000.0)	
R.A.	07:17:32.63
Decl.	+37:44:59.7
X-ray peak position (J2000.0)	
R.A.	07:17:31.65
Decl.	+37:45:18.5
Redshift	0.5458
X-ray temperature (keV)	12.5 ± 0.7
Einstein radius ($''$)	60 ± 3 at $z_s = 2.963$

Notes. The cluster MACS J0717.5+3745($z = 0.5458$) was discovered in the MAssive Cluster Survey (MACS) as described by Reference (1), and its redshift determined by (2). The optical cluster center is defined as the center of the bright red-sequence selected galaxies. The X-ray center and mean temperature were taken from Reference (3). We note that the mean temperature can vary by larger than the quoted uncertainty between authors since it depends on the exact location of the X-ray center, which is different between (1) and (3).
References. (1) Ebeling et al. 2001; (2) Ebeling et al. 2007; (3) Postman et al. 2012.

most luminous X-ray sources (Ebeling et al. 2007) and strongest Sunyaev–Zel'dovich effect (SZE) signal (Planck Collaboration et al. 2011; Marriage et al. 2011; Vanderlinde et al. 2010). Selection effects are now understood to strongly favor the detection of gas compressed or shocked during cluster collision, as illustrated by hydrodynamical simulations (Ricker & Sarazin 2001; Burns et al. 2008; Molnar et al. 2012).

Large simulations of the growth of structure in the context of the standard cold dark matter (ΛCDM; Komatsu et al. 2009) cosmological model have generated increasingly accurate predictions for the evolution of the cluster mass function, extending to a limiting halo mass of approximately $2 \times 10^{15}\ M_{\odot}$ (Neto et al. 2007; Duffy et al. 2008; Zhao et al. 2009; Bhattacharya et al. 2011). The number density of very massive clusters is predicted to change relatively rapidly at low redshift, $z < 1.0$, where the evolution is principally sensitive to the cosmological matter density, Ω_m. To a second order, one may hope to examine the constancy with redshift expected for the "dark-energy" density (Allen et al. 2004; Mantz et al. 2008, 2010b; Schmidt & Allen 2007) and test for self-consistency of general relativity (Rapetti et al. 2010). Presently, however, there are only indirect determinations of the masses of statistical samples of clusters, selected by X-ray means (Ebeling et al. 2000, 2001; Vikhlinin et al. 2009a), and numbering only less than ∼300 clusters, with masses mostly derived from uncertain X-ray scaling relations (Mantz et al. 2010a; Vikhlinin et al. 2006). Although these studies have not yet challenged the standard model (Mantz et al. 2010b; Vikhlinin et al. 2009b), much larger lensing-based surveys of clusters will eventually provide much more detail, in particular, the wide area Subaru/Hyper Suprime-Cam survey (Takada 2010), and later Big-BOSS (Schlegel et al. 2009), LSST (Ivezic et al. 2008), Euclid (Laureijs et al. 2011), and WFIRST (Green et al. 2012).

Despite the lack of lensing-based cluster mass functions, we may progress by exploring the most extreme clusters (Owers et al. 2011; Waizmann et al. 2012a; Colombi et al. 2011), in particular the most distant (Hoyle et al. 2011), because of the exponential sensitivity of the cluster mass function to the growth of structure (Bahcall et al. 1995; Chongchitnan & Silk 2012). Anomalously large masses have been claimed for clusters at $z \lesssim 1.5$ (Rosati et al. 2009; Jee et al. 2009; Santos et al. 2011; Foley et al. 2011; Tozzi et al. 2013). At lower redshifts, accurate full strong+weak lensing total masses were measured for the massive clusters such as A370 ($z = 0.375$) and RX J1347.5 ($z = 0.45$), of the order of $\approx$2–3 $\times 10^{15}\ M_{\odot}$ (Broadhurst et al. 2008; Umetsu et al. 2011a). These clusters were selected from all-sky X-ray surveys (Ebeling et al. 2000, 2001, 2010), so that although the masses are larger and their redshifts are lower, the degree of tension with ΛCDM is not extreme (Waizmann et al. 2012a). At the present time, no individual cluster has been uncovered that strains the credibility of the standard ΛCDM model.

Mapping the mass distribution in clusters has provided insight into the physics that govern dark matter (DM), the main mass component in the universe whose nature is largely unknown. The iconic "Bullet" cluster (Markevitch et al. 2002; Clowe et al. 2004) is an example of a post-merger cluster collision phase, where the diffuse gas component has been separated by ram-pressure from the DM and galaxies (Springel & Farrar 2007; Mastropietro & Burkert 2008), whereas lensing shows that the DM and the galaxies are still spatially coincident (Clowe et al. 2006). This system serves to show that DM is effectively collisionless in nature. Subsequently, several new examples of bullet-like clusters have since been discovered with large-scale supersonic shock fronts (Markevitch et al. 2005; Menanteau et al. 2012; Russell et al. 2010; Korngut et al. 2011; Macario et al. 2011; Owers et al. 2011; Merten et al. 2011; van Weeren et al. 2012), which are hard to reconcile with the expected pairwise velocity distribution of colliding galaxy clusters, where relative impact velocities in excess of 2000 km s^{-1} are unlikely in the context of ΛCDM (Lee & Komatsu 2010; Thompson & Nagamine 2012).

To shed new light on these mysteries of DM and test structure formation models with unprecedented precision, the Cluster Lensing And Supernova survey with Hubble (CLASH; Postman et al. 2012),[25] a 524-orbit *Hubble Space Telescope* (*HST*) multi-cycle treasury program, has been in progress to couple the lensing power of 25 massive clusters ($M_{\rm vir} = 5$–$30 \times 10^{14}\ M_{\odot}$, $\bar{z}_{\rm med} = 0.4$) with *HST* in 16 passbands with full UV/optical/IR coverage, complemented by Subaru wide-field imaging capabilities (e.g., Umetsu et al. 2011a, 2011b). Importantly, 20 CLASH clusters were X-ray selected to be relatively relaxed, in order to examine the concentration–mass relation for a sample with no strong selection bias toward high-concentration clusters. A further sample of five clusters were selected by their high lensing magnification properties, with the goal of detecting and studying high-redshift background galaxies magnified by the cluster potential.

MACS J0717.5+3745 (hereafter, MACSJ0717; $z = 0.5458$) is one of the CLASH high-magnification clusters, and was originally detected by its X-ray emission, as part of the MAssive Cluster Survey (MACS; Ebeling et al. 2001) and independently in the radio (Edge et al. 2003). The cluster has the highest X-ray temperature in the MACS sample ($k_B T_X = 11.6$ keV; Ebeling et al. 2007; also see Table 1), and has since been revealed as one of the most dynamically disturbed clusters known. In the core of this cluster, a complex four-component merging activity has been inferred from optical, X-ray, and internal dynamics (Ma et al. 2008, 2009). Low-frequency radio observations reveal very complex diffuse radio emission (Edge et al. 2003; van Weeren et al. 2009; Bonafede et al. 2009), indicative of a radio

[25] http://www.stsci.edu/~postman/CLASH

relic or halo, and thought to be a signature of major mergers and common to many of the distant MACS clusters where large-scale supersonic shocks are found (Bonafede et al. 2012). High-speed gas motion within MACSJ0717 is also tentatively inferred from dynamical data in a large spectroscopic study, where structural components were defined on the basis of X-ray emission peaks (Ma et al. 2009). This high relative velocity has been confirmed in the multi-frequency SZE measurements of Mroczkowski et al. (2012), which deviate from a thermal SZE spectrum in a way that is consistent with kinetic SZE emission.

A strong-lensing (SL) analysis for this cluster has uncovered a complex elongated tangential critical curve encompassing the central substructures (Zitrin et al. 2009a; Limousin et al. 2012). In terms of the critical area, this cluster has the largest SL area, with an equivalent Einstein radius of, $\theta_E = 55'' \pm 3''$ (at $z_s = 2.963$), and an extremely large mass inside this region, $M_{2D}(<\theta_E) \sim 7 \times 10^{14}\, M_\odot$ (Zitrin et al. 2009a) was deduced. It has been argued that the size of the Einstein radius here may be inconsistent with ΛCDM (Zitrin et al. 2009a; Meneghetti et al. 2011). However, some studies (e.g., Oguri & Blandford 2009; Waizmann et al. 2012b) showed that it can be explained as an extreme case in the context of the lens orientation or other effects. On the larger scale, MACSJ0717 was shown to be part of a filamentary structure from galaxy distributions (Ebeling et al. 2004), and from weak-lensing (WL; Jauzac et al. 2012), possibly spanning 4 Mpc in length.

In this paper, we aim to quantify the complex mass properties of MACSJ0717 and its surrounding large-scale structure (LSS) by employing a comprehensive weak and SL analysis based on deep, wide-field Subaru $BVR_ci'z'$ imaging, combined with our recent CLASH *HST* imaging. We use our methods to derive a robust total mass estimate, and calculate meaningful constraints on the existence of such rare high-mass peaks in a ΛCDM cosmology. The paper is organized as follows. In Section 2, we describe the observational dataset, its reduction, and WL shape measurements. In Section 3, we describe the selection of cluster and background galaxies for WL analysis. In Section 4, we present the WL analysis using Subaru observation. In Section 5, we present improved SL analysis using our new CLASH *HST* observations, and in Section 6, we present a complementary WL analysis using the *HST* observations. In Section 7, we derive cluster mass profiles from lensing, combining SL with WL shear and magnification measurements, and in Section 8, we present the cluster mass distribution spanning both large scales and zooming in on the core, and constrain individual mass peaks using a multi-halo modeling approach. In Section 9, we discuss our lensing mass properties, compare with complementary X-ray and SZE measurements, and contrast the cluster total mass we derive with predictions from ΛCDM cosmology using extreme value statistics. Finally, a summary of our work is given in Section 10.

Throughout this paper, we use the AB magnitude system, and adopt a concordance ΛCDM cosmology with $\Omega_m = 0.3$, $\Omega_\Lambda = 0.7$, and $H_0 = 100\,h$ km s^{-1} Mpc^{-1} with $h = 0.7$. In this cosmology, $1'$ corresponds to 268 kpc $h^{-1} = 383$ kpc at the cluster redshift, $z = 0.5458$. All quoted errors are 68.3% confidence limits (CL) unless otherwise stated. The center is taken as the mean location of red-sequence selected cluster members, R.A. = 07:17:32.63, decl. = +37:44:59.7 (J2000.0).

2. SUBARU+CFHT OBSERVATIONS

In this section, we present the data reduction and analysis of MACSJ0717 based on deep Subaru+CFHT multi-color images (Section 2.1). We briefly describe our WL shape measurement procedure in Section 2.2.

Table 2
Subaru/Suprime-Cam + CFHT/MegaPrime Data

Filter	Exposure Time[a] (ks)	Seeing[b] (arcsec)	$m_{\rm lim}$[c] (AB mag)
u^*	19.63	0.94	26.1
B	3.84	0.95	26.6
V	2.16	0.69	26.4
R_C[d]	2.22	0.79	26.1
i'	0.45	0.96	25.4
z'	5.87	0.85	25.6
J	0.9	0.73	22.7
K_S	0.5	0.54	23.0

Notes.
[a] Total exposure time.
[b] Seeing FWHM in the full stack of images.
[c] Limiting magnitude for a 3σ detection within a $2''$ aperture.
[d] Band used for WL shape measurements.

2.1. Data Reduction and Photometry

We analyze deep $BVR_ci'z'$ images of MACSJ0717 observed with the wide-field camera Suprime-Cam ($34' \times 27'$; Miyazaki et al. 2002) at the prime focus of the 8.3 m Subaru Telescope. We observed the cluster on the night of 2010 March 17, in B, R_C, z', to augment shallower observations that existed in the Subaru archive, SMOKA.[26] Some of the archival data for this cluster were taken as part of the "Weighing the Giants" program (von der Linden et al. 2012). The seeing full-widths at half-maximum (FWHMs) in the co-added mosaic images are $0\farcs95$ in B (3.84 ks), $0\farcs69$ in V (2.16 ks), $0\farcs79$ in R_C (2.22 ks), $0\farcs96$ in i' (0.45 ks), and $0\farcs85$ in z' (5.87 ks) with $0\farcs20$ pixel^{-1}, covering a field of approximately $36' \times 34'$. The limiting magnitudes are obtained as $B = 26.6$, $V = 26.4$, $R_C = 26.1$, $i' = 25.4$, and $z' = 25.6$ mag for a 3σ limiting detection within a $2''$ diameter aperture.

To improve the accuracy of our photometric redshifts, we also include UV observations from the Megaprime/MegaCam in the u^*-band and near-IR observations from the WIRCAM in the J, K_s-bands on the Canada–France–Hawaii Telescope (CFHT), available from the CFHT archive.[27] Although shallower, and in the case of near-IR data the coverage is only of the inner $15' \times 15'$, these extra bands add important information to help better constrain the spectral energy distribution (SED) of galaxies with degenerate fits.

The observation details of MACSJ0717 are listed in Table 2. Figure 1 shows a $u^*BVR_ci'z'$ composite color image of the cluster central $28' \times 28'$, produced automatically using the publicly available Trilogy software (Coe et al. 2012).[28] We overlay it with the DM map determined from WL (white contours, see Section 8) and the smoothed X-ray luminosity map (red contours, see Section 9.2).

Our reduction pipeline derives from Nonino et al. (2009) and SDFRED (Ouchi et al. 2004; Yagi et al. 2002) and has been optimized for accurate photometry and WL shape measurements.

[26] http://smoka.nao.ac.jp
[27] This research used the facilities of the Canadian Astronomy Data Centre operated by the National Research Council of Canada with the support of the Canadian Space Agency.
[28] http://www.stsci.edu/~dcoe/trilogy/

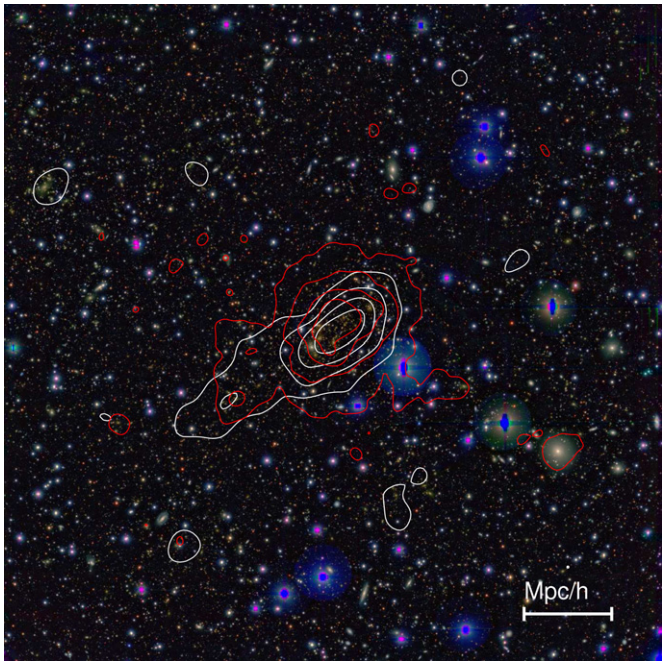

Figure 1. $28' \times 28'$ CFHT u^*+Subaru $BVR_c i'z'$ composite color image showing the galaxy cluster MACSJ0717 ($z = 0.548$). Overlaid are the surface mass density map reconstructed from our Subaru WL analysis (white contours) and the X-ray brightness map from *XMM-Newton* observations (red contours). North is up and east is to the left.

(A color version of this figure is available in the online journal.)

Standard reduction steps include bias subtraction, flat-field correction (super-flat averaged from all exposures of the same night where objects have been masked), and point-spread function (PSF) matching between exposures in the same band (if PSF variation is evident) as we normally use multi-epoch images taken under different conditions. Masking of saturated star trails and other artifacts is then applied.

To obtain an accurate astrometric solution for Subaru observations, we retrieved processed MegaCam *r*-band (Filter Number: 9601) images from the CFHT archive and used it as a wide-field reference image. A source catalog was created from the co-added MegaCam *r* image, using the Two Micron All Sky Survey catalog[29] as an external reference catalog. The extracted *r* catalog has been used as a reference for the SCAMP software (Bertin 2006) to derive an astrometric solution for the Suprime-Cam and other CFHT images. We do not use the CFHT *r*-band image in our photometry as the band is overlapping the Subaru R_C band, but with much lower resolution and depth, and therefore, does not carry added information.

For an accurate measure of photometry, we first smear the single exposures of the same band to the worst seeing. This step is done by using SDFRED/PSFMATCH procedure, after suitable point-like sources have been previously selected. The WL band is chosen to be the band with a combination of best seeing and deepest observation, R_C in this case (see Table 2).

Finally, the SWARP software (Bertin et al. 2002) is utilized to stack the single exposures on a common world coordinate system grid with pixel-scale of 0.″2 using the accurate registration that was achieved in the previous step. This assures minimal distortion of the final image. Note that for the WL band, we separately stack data collected at different epochs and different camera rotation angles.

The photometric zero-points for the co-added Suprime-Cam images were derived from a suitable set of reference stars identified in common with the calibrated MegaCam data. These zero-points were refined in two independent ways: first, by comparing with the *HST*/ACS magnitudes of cluster elliptical-type galaxies, translated to Subaru magnitudes using an elliptical SED template with the BPZ code; subsequently, by fitting SED templates with the BPZ code (Bayesian photometric redshift estimation; Benítez 2000; Benítez et al. 2004) to Subaru photometry of 12 galaxies having measured spectroscopic redshifts from the literature[30] (Limousin et al. 2012) and calculating model magnitudes. This leads to a final photometric accuracy of ∼0.01 mag in all passbands (see also Section 3.3).

The eight-band $u^*BVR_c i'z'JK_S$ photometry catalog was then measured using SExtractor (Bertin & Arnouts 1996) in dual-image mode on PSF-matched images created by ColorPro (Coe et al. 2006), where a combination of $B + V + R + z'$ bands were used as a deep detection image (we exclude the i' band which is of lesser quality). The stellar PSFs were measured from a combination of 100 stars per band and modeled using IRAF routines.

2.2. Subaru Shape Measurement

For shape measurements, we use our well-tested WL analysis pipeline based on the IMCAT package (Kaiser et al. 1995, KSB hereafter), incorporating modifications and improvements developed and outlined in Umetsu et al. (2010). Our KSB+ implementation has been applied extensively to Subaru cluster observations (e.g., Broadhurst et al. 2005b, 2008; Umetsu et al. 2007, 2009, 2010, 2011a, 2011b; Umetsu & Broadhurst 2008; Okabe & Umetsu 2008; Medezinski et al. 2010, 2011; Zitrin et al. 2011, 2013; Coe et al. 2012; Umetsu et al. 2012). Full details of our CLASH WL analysis pipeline are presented in Umetsu et al. (2012).

Based on simulated Subaru Suprime-Cam images (see Section 3.2 of Oguri et al. 2012; Massey et al. 2007a), we found in our earlier work (Umetsu et al. 2010, 2012) that the WL signal can be recovered with $|m| \simeq 5\%$ of the multiplicative shear calibration bias (as defined by the STEP project: see Heymans et al. 2006; Massey et al. 2007a), and $c \sim 10^{-3}$ of the residual shear offset, which is about one order of magnitude smaller than the typical distortion signal in cluster outskirts ($|g| \sim 10^{-2}$). Accordingly, we include in our analysis a calibration factor of $1/0.95$ as $g_i \rightarrow g_i/0.95$ to account for residual calibration.[31]

In this analysis, we use the R_C-band data taken in 2005 and 2010, which have the best image quality in our datasets, taken in fairly good seeing conditions. Two separate co-added R_C-band images are created, one from 2005 (with a total of 450 s, observer Yasuda) and one from 2010 (with a total of 2160 s, observed by us on 2010 March). We do not smear the single exposures before

[29] This publication makes use of data products from the Two Micron All Sky Survey, which is a joint project of the University of Massachusetts and the Infrared Processing and Analysis Center/California Institute of Technology, funded by the National Aeronautics and Space Administration and the National Science Foundation.

[30] This research has made use of the NASA/IPAC Extragalactic Database (NED) which is operated by the Jet Propulsion Laboratory, California Institute of Technology, under contract with the National Aeronautics and Space Administration.

[31] Our earlier CLASH weak-lensing work in Zitrin et al. (2011), Umetsu et al. (2012), and Coe et al. (2012) did not include the 5% residual correction. Our forthcoming CLASH sample analysis papers will include the 5% correction factor.

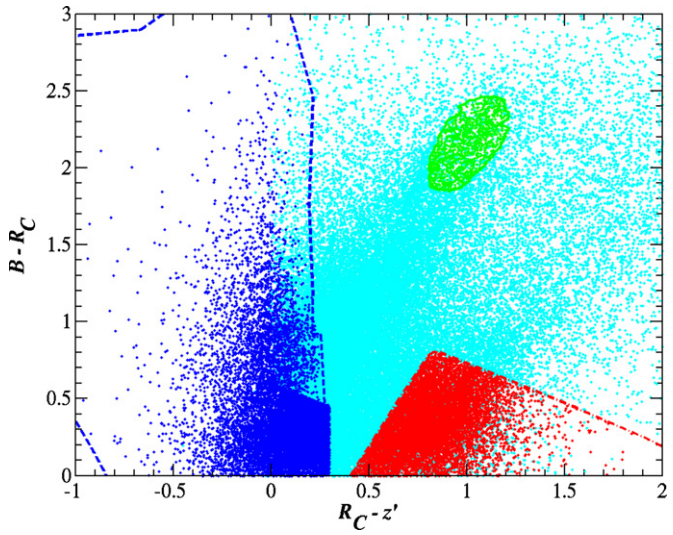

Figure 2. "Blue" and "red" background galaxies are selected for WL analysis (lower left blue dashed and right red dot-dashed contours, respectively) based on Subaru B, R_C, z' color–color–magnitude selection. All galaxies (cyan) are shown in the diagram. At small clustercentric radius, an overdensity of cluster galaxies defines our "green" sample (green solid contour), comprising mostly the red sequence of the cluster and some blue trail of later type cluster members. The background samples are well isolated from the green region and satisfy other criteria as discussed in Section 3.2.

(A color version of this figure is available in the online journal.)

stacking (as done for photometric measurements), so as not to degrade and destroy the WL information derived from the shapes of galaxies. A shape catalog is created for each epoch separately, and the catalogs themselves are then combined by properly weighting and stacking the calibrated distortion measurements for galaxies in the overlapping region. The combination of both epochs increases the number of measured galaxy shapes and improves the statistical measurement, while not degrading the quality of the shape measurement due to different seeing and anisotropy at different observing epochs.

3. SAMPLE SELECTION

For an undiluted WL detection, we need to carefully select a pure sample of background galaxies. In order to further explore the distribution of the cluster galaxies, we also identify the cluster members population. We use the B, R_c, z' Subaru imaging which spans the full optical wavelength range to perform color–color (CC) selection of cluster and background samples, as demonstrated by Medezinski et al. (2010) and detailed below.

3.1. Cluster Sample Selection

In Figure 2, we show the $B - R_C$ versus $R_C - z'$ distribution of all galaxies to our limiting magnitude (cyan). To identify our cluster-dominated area in this CC space, we also plot up $B - R_c$ versus $R_C - z'$ only of galaxies with small projected distance $R < 3'$ ($\lesssim$1 Mpc at $z_l = 0.546$) from the cluster center. A region is then defined according to a characteristic overdensity in this space (shown as a solid green curve in Figure 2). Then, *all* galaxies within this distinctive region from the full CC diagram define the "green" sample (green points in Figure 2), comprising mostly the red-sequence of the cluster and a blue trail of later-type cluster members. We note that the small overdensity seen bluer (lower-left, $B - R_C$, $R_C - z' \sim 0.7$) than our green sample does not lie at the same redshift of the cluster and is not a bluer population that is part of the cluster, but is in fact comprised of early-type galaxies lying in the foreground of the cluster, at about $z \sim 0.33$, which we will discuss further as part of our multi-halo mass modeling (Section 8.2).

The number density profile of the green sample is steeply rising toward the center (Figure 6, green crosses). The low number density at large clustercentric radius is indicative of negligible contamination of background galaxies of this sample. The WL signal for this population is found to be consistent with zero at all radii (Figure 5, green crosses), also indicating the reliability of our procedure. For this population of galaxies, we find a mean photometric redshift of $\langle z_{\rm phot} \rangle \approx 0.56$ (see Section 3.3), consistent with the cluster redshift. Importantly, the green sample marks the region that contains a majority of unlensed galaxies, relative to which we select our background samples, as summarized below.

3.2. Background Sample Selection

A careful background selection is critical for a WL analysis so that unlensed cluster members and foreground galaxies do not dilute the true lensing signal of the background (Broadhurst et al. 2005b; Medezinski et al. 2007, 2010; Umetsu & Broadhurst 2008). This dilution effect is simply to reduce the strength of the lensing signal when averaged over a local ensemble of galaxies (by a factor of 2–5 at $R \lesssim 400\,{\rm kpc}\,h^{-1}$; see Figure 1 of Broadhurst et al. 2005b), particularly at small radii where the cluster is relatively dense, in proportion to the fraction of unlensed galaxies whose orientations are randomly distributed.

We use the background selection method of Medezinski et al. (2010) to define undiluted samples of background galaxies, which relies on empirical correlations for galaxies in color–color–magnitude space derived from the deep Subaru photometry, by reference to evolutionary tracks of galaxies (for details, see Medezinski et al. 2010; Umetsu et al. 2010) as well as to the deep photometric-redshift survey in the COSMOS field (Ilbert et al. 2009).

For MACSJ0717, we have a wide wavelength coverage ($BVR_ci'z'$) of Subaru/Suprime-Cam. We therefore make use of the $(B - R_c)$ versus $(R_c - z')$ CC diagram to carefully select two distinct background populations which encompass the red and blue branches of galaxies. We limit the red sample to $z' < 25$ mag in the reddest band, corresponding approximately to a 5σ limiting magnitude within $2''$ diameter aperture. We extend the magnitude limit of the blue samples further to $z' < 26$ mag, where the number density of galaxies grows significantly higher, especially for bluer galaxies whose faint-end slope of the luminosity function is rising, giving a much improved WL statistical measurement.

For the background samples, we define conservative color limits, where no evidence of dilution of the WL signal is visible, to safely avoid contamination by unlensed cluster members and foreground galaxies. The color boundaries of our "blue" and "red" background samples are shown in Figure 2. For both the blue and red samples, we find a consistent, rising WL signal (see Section 4.1) all the way to the center of the cluster, as shown in Figure 5.

As a further consistency check, we also plot in Figure 6 the galaxy surface number density as a function of clustercentric radius, $n(\theta)$, for the blue and red samples. As can be seen, no clustering is observed toward the center for the background samples, which demonstrates that there is no significant contamination by cluster members in these samples. The red sample systematically decreases in projected number density toward

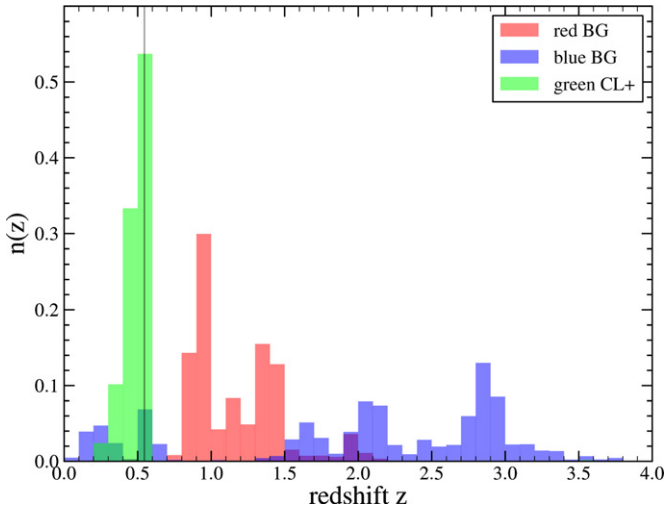

Figure 3. Redshift distributions of the CC-selected green, red, and blue samples using the BPZ photo-z's based on Subaru+CFHT imaging. The cluster redshift is marked with a black line.

(A color version of this figure is available in the online journal.)

Table 3
Galaxy Color Selection

Sample	Magnitude Limits[a] (AB mag)	N	n_g[b] (arcmin^{-2})	$\langle z_s \rangle$[c]
Red	$21 < z' < 25$	10490	9.6	1.21
Green	$z' < 24$	1252	1.3	0.49/0.54
Blue	$22.5 < z' < 26$	11998	11.5	2.23

Notes.
[a] Magnitude limits for the galaxy sample.
[b] Mean surface number density of source background galaxies.
[c] Mean photometric redshift of the sample obtained with the BPZ code.

the cluster center, caused by the lensing magnification effect. A more quantitative magnification analysis is given in Section 4.2.

To summarize, our CC selection criteria yielded a total of $N = 10{,}490$, 1252, and 11,998 galaxies, for the red, green, and blue photometry samples, respectively (see Table 3). For our WL distortion analysis, we have a subset of 4856 and 4738 galaxies in the red and blue samples (with usable R_C shape measurements), respectively (see Table 4).

3.3. Depth Estimation

The lensing signal depends on the source redshift z_s through the distance ratio $\beta(z_s) = D_{ls}/D_s$, where D_{ls}, and D_s are the angular diameter distances between the lens and the source, and the observer and the source, respectively. We thus need to estimate and correct for the respective depths $\langle\beta\rangle$ of the different galaxy samples when converting the observed lensing signal into physical mass units.

For this, we utilize BPZ to measure photometric redshifts (photo-zs) $z_{\rm phot}$ using our deep Subaru+CFHT $u^*BVR_ci'z'JK_s$ photometry (Section 2.1). BPZ employs a Bayesian inference where the redshift likelihood is weighted by a prior probability, which yields the probability density $P(z, T|m)$ of a galaxy with apparent magnitude m of having certain redshift z and spectral type T. In this work, we used a new library (N. Benitez 2012, in preparation) composed of 10 SED templates originally from PEGASE (Fioc & Rocca-Volmerange 1997) but recalibrated using the FIREWORKS photometry and spectroscopic redshifts

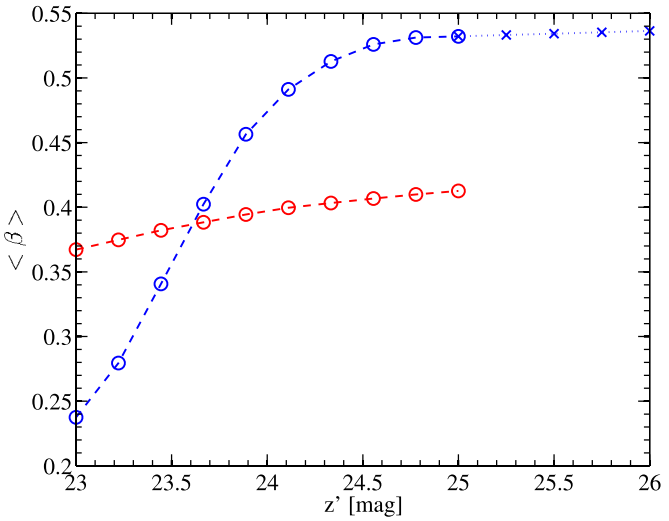

Figure 4. Lensing depth (D_{ls}/D_s) as a function of Subaru z'-band limiting magnitude for the red and blue background samples, as estimated from the photometric redshifts of COSMOS to $z' < 25$ (circles). In order to estimate the depth of the blue sample to its limiting magnitude of $z' < 26$, we extrapolate the curve (x's).

(A color version of this figure is available in the online journal.)

from Wuyts et al. (2008) to optimize its performance. This library includes five templates for elliptical galaxies, two for spiral galaxies, and three for starburst galaxies. In our depth estimation, we utilize BPZ's ODDS parameter, which measures the amount of probability enclosed within a certain interval Δz centered on the primary peak of the redshift probability density function, serving as a useful measure to quantify the reliability of photo-z estimates.

We only consider galaxies from the WL-matched catalogs, as those are the galaxies from which we estimate the lensing signal and finally, the mass profile. To make this estimate more robust, we use galaxies for which the photo-z was determined using all available eight bands. We show the normalized redshift distribution of these galaxies in each of the green, red, and blue samples in Figure 3. Still, since only 12 spectroscopic redshifts are publicly available in this field, it is difficult to estimate the reliability of our photo-z's. Therefore, we further compare our results with the more reliably estimated depths we derive from the COSMOS catalog (Ilbert et al. 2009), which has robust photometry and photo-z measurements for the majority of galaxies with $i' < 25$ mag. For each sample, we apply the same CC selection to the COSMOS photometry and obtain the redshift distribution $N(z)$ of field galaxies. Since COSMOS is only complete to $i' < 25$ mag, we derive the mean depth as a function of magnitude (Figure 4) up to that limit, and extrapolate to our sample limiting magnitude, $z' = 25$ in the case of the red sample and $z' = 26$ in the case of the blue sample.

For each background population, we calculate a weighted mean of the distance ratio β (mean lensing depth) as

$$\langle\beta\rangle = \frac{\int dz\, w(z) N(z) \beta(z)}{\int dz\, w(z) N(z)}, \quad (1)$$

where $w(z)$ is a weight factor; w is taken to be the Bayesian ODDS parameter for the BPZ method, and $w = 1$ otherwise. The sample mean redshift $\langle z_s \rangle$ is defined similarly to Equation (1).

In Table 4, we summarize the mean depths $\langle\beta\rangle$ and the effective source redshifts $z_{s,\rm eff}$ for our background samples.

Table 4
Galaxy Samples for WL Shape Measurements

Sample	N	n_g[a] (arcmin^{-2})	σ_g[b]	$z_{s,\mathrm{eff}}$[c]		$\langle D_{ls}/D_s\rangle$[d]	
				MACSJ0717	COSMOS	MACSJ0717	COSMOS
Red	4856	5.65	0.41	1.1	1.08	0.43	0.42
Blue	4738	5.6	0.42	1.89	1.56	0.59	0.55
Blue+red	9594	11.2	0.41	1.26	1.27	0.48	0.48

Notes.
[a] Mean surface number density of galaxies.
[b] Mean rms error for the shear estimate per galaxy, $\sigma_g \equiv (\overline{\sigma_g^2})^{1/2}$.
[c] Effective source redshift corresponding to the mean depth $\langle\beta\rangle$ of the sample.
[d] Distance ratio averaged over the redshift distribution of the sample, $\langle\beta\rangle$.

For each background sample, we obtained consistent mean-depth estimates $\langle\beta\rangle$ (within 2%) using the BPZ- and COSMOS-based methods. In the present work, we adopt a conservative uncertainty of 5% in the mean depth for the combined blue and red sample of background galaxies, $\langle\beta(\mathrm{back})\rangle = 0.48 \pm 0.03$, which corresponds to $z_{s,\mathrm{eff}} = 1.26 \pm 0.1$. We marginalize over this uncertainty when fitting parameterized mass models to our WL data.

4. SUBARU WEAK-LENSING ANALYSIS

In this section, we describe the WL analysis based on our deep Subaru imaging data. In Section 4.1, we derive cluster lens distortion, and in Section 4.2, we derive the magnification radial profiles from the data.

4.1. Tangential Distortion Analysis

The shape distortion of an object is described by the complex reduced-shear, $g = g_1 + ig_2$, where the reduced-shear is defined as (in the subcritical regime; see, e.g., Bartelmann & Schneider 2001)

$$g_\alpha \equiv \gamma_\alpha/(1-\kappa), \tag{2}$$

where γ is the complex gravitational shear field and is non-locally related to the convergence, $\kappa = \Sigma/\Sigma_{\mathrm{crit}}$, which is the surface mass density in units of the critical surface-mass density for lensing, $\Sigma_{\mathrm{crit}} = (c^2/4\pi G D_l)\beta^{-1}$. The tangential component of the reduced-shear, g_+, is used to obtain the azimuthally averaged distortion due to lensing, and computed from the distortion coefficients (g_1, g_2):

$$g_+ = -(g_1\cos 2\theta + g_2 \sin 2\theta), \tag{3}$$

where θ is the position angle of an object with respect to the cluster center. The uncertainty in the object g_+ measurement is $\sigma_+ = \sigma_g/\sqrt{2} \equiv \sigma$ in terms of the rms error σ_g for the complex reduced-shear measurement. For each galaxy, σ_g is the variance for the reduced shear estimate computed from 50 neighbors identified in the r_g–R_C plane. To improve the statistical significance of the distortion measurement, we calculate the weighted average of g_+

$$g_{+,i} \equiv g_+(\theta_i) = \left[\sum_{k\in i} w_{(k)}\, g_{+(k)}\right]\left[\sum_{k\in i} w_{(k)}\right]^{-1}, \tag{4}$$

where the index k runs over all objects located within the ith radial bin with a weighted center of θ_i, and $w_{(k)}$ is the weight for the kth object,

$$w_{(k)} = 1/\left(\sigma^2_{g(k)} + \alpha^2\right), \tag{5}$$

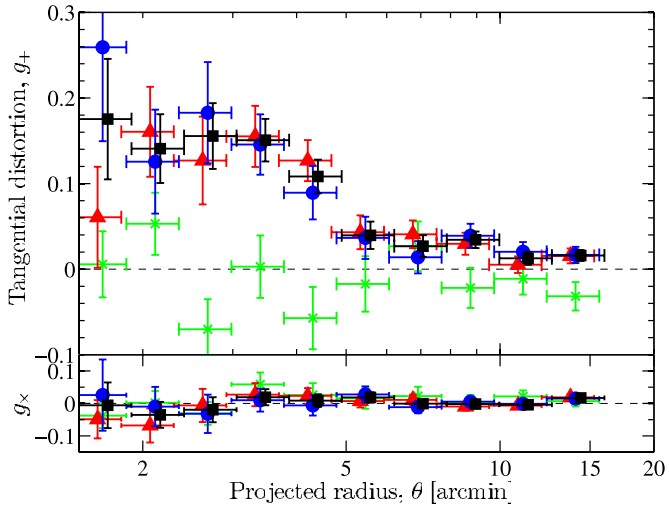

Figure 5. Azimuthally averaged radial profiles of the tangential reduced-shear g_+ (upper panel) and the 45° rotated (×) component $g_\times$ (lower panel) for our red (triangles), blue (circles), green (crosses), and blue+red (squares) galaxy samples. The symbols for the red and blue samples are horizontally shifted for visual clarity. For all of the samples, the ×-component is consistent with a null signal detection well within 2σ at all radii, indicating the reliability of our distortion analysis.
(A color version of this figure is available in the online journal.)

where α^2 is the softening constant variance. We choose $\alpha = 0.4$, which is a typical value of the mean rms $\bar{\sigma}_g$ over the background sample. The uncertainty in $g_{+,i}$ is calculated from a bootstrap error analysis (for details, see Umetsu et al. 2012). Since WL only induces curl-free tangential distortions, the 45° rotated component, $g_\times = -(g_2\cos 2\phi - g_1 \sin 2\phi)$, is expected to vanish. It is therefore useful as a check for systematic errors.

In Figure 5, we plot the radial profile of g_+ of the green, red, and blue samples defined above. The black points represent the red+blue combined sample (also shown in Figure 8, upper panel), showing the best estimate of the lensing signal, which is detected at 11.6σ significance over the full radial range. The red and blue sample profiles rise continuously toward the center of the cluster, and agree with each other within the errors, except at the very central bin, $\theta \lesssim 2'$, where measurements are approaching the nonlinear regime, given the extremely elliptical shape of the tangential critical curve (see Figure 1 of Zitrin et al. 2009a). The overall rising trend and agreement demonstrate that both the red and blue samples are dominated by background galaxies and are not contaminated by the cluster at all radii. The g_+ profile of the green sample agrees with zero at all radii. The measured zero level of tangential distortion reinforces our CC selection of the green sample to consist mostly of cluster members.

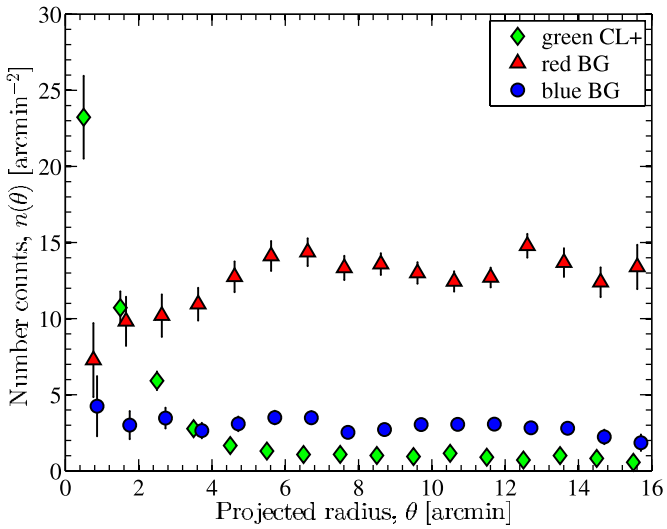

Figure 6. Surface number density profiles $n(\theta)$ of Subaru $BR_c z'$-selected samples of galaxies. The red (triangles) and blue (circles) samples comprise background galaxies, and the green (crosses) sample comprises mostly cluster galaxies, as is evident by their steeply rising number counts toward the center. See also Figure 8.

(A color version of this figure is available in the online journal.)

4.2. Magnification-bias Analysis

We follow the prescription of Umetsu et al. (2011a) to measure the magnification bias signal as a function of distance from the cluster center, which depends on the intrinsic slope of the luminosity function of background sources s, as

$$n_\mu(\boldsymbol{\theta}) = n_0 \mu(\boldsymbol{\theta})^{2.5s-1}, \quad (6)$$

where $n_0 = dN_0(<m_{\rm cut})/d\Omega$ is the unlensed mean number density of background sources for a given magnitude cutoff $m_{\rm cut}$, approximated locally as a power-law cut with slope, $s = d\log_{10} N_0(<m)/dm > 0$. We use the red sample of background galaxies (Section 3.2), for which the intrinsic count slope s at faint magnitudes is relatively flat, $s \sim 0.1$, so that a net count depletion results (Broadhurst et al. 2005b; Umetsu & Broadhurst 2008; Umetsu et al. 2010, 2011a). In contrast, the blue background population has a steeper intrinsic count slope close to the lensing invariant slope ($s = 0.4$).

Here we use the approach developed in Umetsu et al. (2011a) to measure the azimuthally averaged surface number density profile of the red galaxy counts, $n_{\mu,i} \equiv n_\mu(\theta_i)$ (red triangles in Figure 6), taking into account and correcting for masking of background galaxies due to bright cluster galaxies (BCGs), foreground objects, and saturated objects. The errors $\sigma_{\mu,i}$ for $n_{\mu,i}$ include both contributions from Poisson errors in the counts and contamination by intrinsic clustering of red background galaxies. The normalization and slope parameters for the red sample are reliably estimated outside the lensed region, by virtue of the wide-field imaging with Subaru/Suprime-Cam. We find $n_0 = 13.3 \pm 0.3$ galaxies acrmin^{-2} and $s = 0.123 \pm 0.048$.

In the bottom panel of Figure 8, we show the measured magnification profile from our flux-limited sample of red background galaxies ($z' < 25$ mag; see Table 3) with and without the masking correction applied (red circles and green crosses, respectively). A clear depletion of the red counts is seen in the central, high-density region of the cluster and detected out to $\lesssim 4'$ from the cluster center. The radially integrated significance of the detection of the depletion signal is 5.3σ.

The high-level WL shear and magnification profile we derived here can be combined together to reconstruct the underlying mass profile. However, to better resolve the core of the profile, we require further constraints which are enabled by SL. Therefore, we derive the SL mass profile in the next section.

5. *HST* STRONG-LENSING ANALYSIS

For a massive cluster, the weak- and strong-regimes contribute similar logarithmic coverage of the mass profile. Hence, the central SL information is crucial in a cluster lensing analysis (Umetsu et al. 2011a, 2011b, 2012). In this section, we derive an SL model to compare with our WL profile in the overlap region and to combine with WL in deriving the mass reconstruction in Section 7.

First, we summarize our well-tested approach to strong-lens modeling, developed by Broadhurst et al. (2005a) and optimized further by Zitrin et al. (2009b) (see also Zitrin et al. 2013). Briefly, the adopted parameterization is as follows. Cluster members, chosen by a F814W-F555W color criterion, are each represented by a power-law mass density profile. The superposition of all galaxy contributions constitutes the galaxy, lumpy component for the model. This component is then smoothed using a two-dimensional (2D) spline interpolation to comprise the DM component. The two components are then added with a relative weight. In order to allow further degrees of freedom (dof), and higher effective ellipticity of the critical curves, an external shear is added. In total, the method thus includes six basic free parameters: (1) the power-law of the galaxy mass profile; (2) the smoothing (polynomial) degree of the DM component; (3) the relative weight of the galaxy to the DM component; (4) the overall scaling or normalization; (5) the amplitude; and (6) angle of the external shear (for more details see Zitrin et al. 2009b).

Using this method, in Zitrin et al. (2009a), we performed the first SL analysis of this cluster using three-band publicly available *HST* imaging, and found 34 multiple-images from 13 lensed sources, uncovering that MACSJ0717 is the largest known lens. As part of CLASH (Postman et al. 2012), we further observed MACSJ0717 with *HST* in 16 filters with the Advanced Camera for Surveys (ACS) and WFC3/UVIS+IR cameras. We thus revise here our primary multiple image identification, and follow in general the multiple image sets listed in Table 1 of Limousin et al. (2012, hereafter L12), who recently used Zitrin et al.'s (2009a) systems (with the exclusion of three systems, 9–11) and added *five* additional multiple systems which were subsequently verified with the help of the publicly available CLASH WFC3/IR images. Although we agree with most of the identifications and revisions by L12, we determine image 1.5 to be at a different location, R.A. = 07:17:37.393, decl. = +37:45:40.90. We also confirm that this new location significantly improves the SL parametric solution of L12 (M. Limousin 2013, private communication). In addition, although the model suggests these may be counter images of the same source, we omit system 2 from our list, since it strongly deviates from the $D_{\rm ls}/D_{\rm s}$ scaling relation expected, and as determined from visual inspection. Aside from these corrections, here we use 43 multiple-images in total coming from the other 14 sources listed in L12 as our SL constraints. Internal bright knots in some of the images are added as further constraints. We note that since we have sufficient information to constrain the mass model, we do not attempt to find additional multiple images in the current paper, and we leave this for future work, mainly in the framework of the upcoming Frontier Fields program.

We use a several dozen thousand step Monte Carlo Markov Chain (MCMC) minimization in order to find the best-fit solution, defined by the image-plane reproduction χ^2. The advantage of this light-traces-mass (Zitrin et al. 2009a) method is that even very complex systems such as MACSJ0717 are still well fitted by this simple procedure, although it may not be expected to yield an rms as low as in a multi-halo/parametric fit (e.g., L12). Note, however, that even with a somewhat higher rms, the representation is still highly credible as it allowed the identification of many multiple image systems (Zitrin et al. 2009a).

Here, in practice, to allow for more freedom and a better rms, we also leave the relative weight of 10 galaxies to be freely optimized by the MCMC. With this, the final model we present here has an rms of $3\farcs86$ and a χ^2 of $\simeq$334 (with a location error of $\sigma = 1\farcs4$), over 32 dof. The relatively large reduced χ^2 (compared with the reasonable rms) may indicate that in such a complex system, a position error of $1\farcs4$ may be underestimated, not taking into account stronger LSS and complexity effects. Since the best-fit statistical solution defined by the image positions may not always reproduce the multiple images with the right internal shape or orientation, multiple images are then sent to the source plane and back through the lens to test, by eye, the reproduction of other multiple images of the same systems (e.g., Zitrin et al. 2009a, 2009b). Note that only five systems have spectroscopic redshift, so that we use the input from L12 as the predicted redshift of the other systems. We do not leave any of these redshifts to be optimized by the model, which may have further lowered the rms of our model.

We present the azimuthally averaged projected mass density profile from the resulting SL model of MACSJ0717 in Figure 13 (green curve). The density profile shows a remarkably flat core out to $\lesssim$180 kpc h^{-1}, as was noted in previous SL analyses of this cluster (Zitrin et al. 2009a). The shallow profile is in accordance with the non-relaxed appearance of this cluster and reported multiple mass clumps at the core of the cluster. According to our SL model, the total projected mass enclosed within a radius of $60'' \pm 6''$, the effective Einstein radius at $z_s = 2.963$, is $M_{2D}(<60'') = (4.87 \pm 0.35) \times 10^{14}\, M_\odot\, h^{-1}$, which is in good agreement with the mass enclosed within the tangential critical curve, $M_{2D} = (5.5 \pm 0.35) \times 10^{14}\, M_\odot\, h^{-1}$. We now turn to the WL analysis in the next sections in order to recover the mass over the full scale of the cluster.

6. *HST* WEAK-LENSING ANALYSIS

In order to further constrain the mass profile in the cluster center, where the small Subaru number density leads to large uncertainties, we perform a complementary WL analysis of the *HST* 16-band data in the weak regime. Details of our reduction, photometry, and photo-z pipeline were given in previous papers (Postman et al. 2012; Zitrin et al. 2012b; Coe et al. 2012). Here we further produced specialized drizzled images, optimized for WL, consisting of drizzling each visit in the "unrotated" frame of the ACS/WFC3 detectors, using a modified version of the "Mosaicdrizzle" pipeline (described more fully in Koekemoer et al. 2011). This allows accurate PSF treatment that does not compromise the intrinsic shape measurements required by WL pipelines. The RRG (Rhodes et al. 2000) WL shape measurement package was then used to measure shapes in each of six ACS bands (F435W, F475W, F625W, F775W, F814W, and F850LP), and the DEIMOS (Melchior et al. 2011) package was used to measure shapes in the WFC3/IR F160W band. We exclude objects with signal-to-noise ratio (S/N) < 10 and size $<0\farcs1$. All of the shape catalogs were then matched to the deep multi-band photometric catalog and merged where there was more than one shape measurement per object, using its S/N as input weight of each measurement, according to Equation (5) with $\alpha = 0.2$ as the softening kernel in this case.

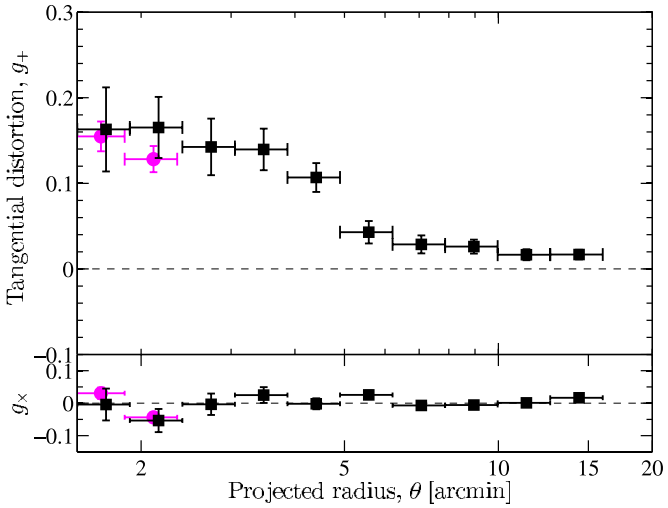

Figure 7. As in Figure 5, we show the tangential distortion profile of the Subaru background sample (black squares), and compare with the *HST*-derived background sample in the central $R < 2\farcm4$ (magenta circles) but outside the critical lensing region, $R > 1\farcm5$. As can be seen, these two complementary datasets give consistent WL signal at the region of overlap, whereas the *HST* points have much smaller errors and therefore provide better constraints.

(A color version of this figure is available in the online journal.)

Since the *HST* field has reliable photometric redshifts measured from 16 bands spanning UV to IR, here we rely on those for a secure selection of background galaxies. We define our background sample as galaxies having $0.8 < z_b < 4$, $z_{b,min} > 0.6$, $z_{b,max} < 5$, $22.5 < m_{F625W} < 27.5$, where z_b is the Bayesian photometric redshift from BPZ, and $z_{b,min}$ and $z_{b,max}$ are the 68% lower and upper bound on the photometric redshift estimate, respectively. To examine the light distribution, we chose an inclusive cluster-member sample based on $|z_b - z_{cl}| < 0.1$, $z_{b,min} > z_{cl}-0.2$, $z_{b,max} < z_{cl}+0.2$, $17 < m_{F625W} < 24.5$. In order to do a simultaneous analysis of the WL signal in both the *HST* and Subaru fields, we need to account for the different redshift distribution of the different populations these two datasets target. We do this by estimating the depth factor, $\beta(z)$, from the *HST* photo-z's. For the *HST* background catalog we estimate $\beta \sim 0.525$, about a $\sim$10% increase in depth relative to the Subaru catalog, estimated at $\beta \sim 0.48$. We apply this relative correction to the *HST* catalog and scale it to match the Subaru catalog.

A significant part of the *HST* region resides inside the tangential critical curve area, and so is super-critical. In order to avoid nonlinear effects in the WL analysis, we examine the tangential distortion profile only at the outer region of *HST*, $1.5 < \theta < 2\farcm5$, to the limit of the data. We present the results in Figure 7, where we overplot the inner two bins (magenta circles) from *HST* that overlap with the same region in the inner Subaru (black squares) profile. The two independent datasets show consistent WL shear signal within the uncertainties, although we note that the *HST* signal does show a slightly decreased level. This may arise from nonlinear effects causing an underestimation of the shear (and possibly also the non-null cross-shear in the second bin), or simple image edge effects due to different filter coverage. However, this level

is still negligible and does not significantly affect our results. We will present the 2D distribution analysis of the *HST* region in Section 8.4, after we first incorporate the *HST*+Subaru WL with *HST* SL information to reconstruct the mass profile over the entire Subaru field of view (FOV) in the next section.

7. RADIAL MASS PROFILE ANALYSIS

7.1. Mass Profile Reconstruction Using One-dimensional Shear and Magnification

We derive the cluster mass profile as a function of clustercentric radius from a joint likelihood analysis of independent WL distortion (g_+), magnification-bias (n_μ), and SL projected mass (m) constraints, $\{g_{+,i}\}_{i=1}^{N_{\rm wl}}$ (Section 4.1), $\{n_{\mu,i}\}_{i=1}^{N_{\rm wl}}$ (Section 4.2), and $\{m_i\}_{i=1}^{N_{\rm sl}}$ (Section 5), respectively, following the Bayesian approach of Umetsu (2013), who extended the *shear-and-magnification* analysis method of Umetsu et al. (2011a) to include the inner SL information. Such a multi-probe approach is critical for improving the accuracy and precision of the cluster lens reconstruction, effectively breaking the mass-sheet degeneracy (see Bartelmann & Schneider 2001; Umetsu et al. 2012). Adding SL information to WL is needed to provide tighter constraints on the inner density profile (e.g., Umetsu & Broadhurst 2008; Umetsu et al. 2011a, 2012). The shear+magnification method of Umetsu et al. (2011a) has been extensively used to reconstruct the projected mass profile in a dozen clusters (Umetsu et al. 2011a, 2012; Zitrin et al. 2011, 2013; Coe et al. 2012). In all cases, we find a good agreement between independent WL and SL mass profiles in the region of overlap.

Briefly summarizing, the model is described by a vector $\boldsymbol{s}$ of parameters containing the discrete convergence profile $\{\kappa_{\infty,i}\}_{i=1}^{N}$, given by $N = N_{\rm wl} + N_{\rm sl}$ binned κ values, and the average convergence enclosed by the innermost aperture radius $\theta_{\rm min}$ for SL mass estimates, $\overline{\kappa}_{\infty,\rm min} \equiv \overline{\kappa}_\infty(<\theta_{\rm min})$, where we have introduced the convergence for a fiducial source in the far background of the cluster, $\kappa_{\infty,i} \equiv \kappa(\theta_i; z_s \to \infty)$. The model $\boldsymbol{s} = \{\overline{\kappa}_{\infty,\rm min}, \kappa_{\infty,i}\}_{i=1}^{N}$ is then specified by a total of $(N+1)$ parameters. Additionally, we account for the uncertainty in the calibration parameters, $\boldsymbol{c} = (w_g, w_\mu, n_0, s)$, namely, the population-averaged lensing strengths for the distortion and magnification measurements (see Table 4), $w_g \equiv \langle\beta(\text{back})\rangle/\beta(z_s \to \infty)$ and $w_\mu \equiv \langle\beta(\text{red})\rangle/\beta(z_s \to \infty)$, the normalization and slope parameters (n_0, s) of the red-background counts (see Section 4.2). The covariance matrix C_{ij} for the profile reconstruction is also constructed and used for calculating the likelihood function of the combined WL+SL observations.

In the present analysis, we calculate the g_+ and n_μ profiles in $N_{\rm wl} = 10$ clustercentric radial bins, spanning the range $\theta = [1.'5, 16']$, with a constant logarithmic radial spacing $\Delta\ln\theta \simeq 0.237$. Additionally, we use our projected mass measurement within a radius of $60''$, $m = M_{\rm 2D}(<60'') = (4.87 \pm 0.35) \times 10^{14}\, M_\odot\, h^{-1}$ ($N_{\rm sl} = 1$), tightly constrained by our detailed strong-lens modeling (Section 5). Note that enclosed masses at the location around the Einstein radius ($\theta_{\rm Ein} \approx 60''$ at $z_s = 2.963$ here) are less sensitive to modeling assumptions and approaches (see Umetsu et al. 2012), serving as a fundamental observable quantity in the SL regime (Coe et al. 2010). Hence, we have a total of $N_{\rm tot} = 2N_{\rm wl} + N_{\rm sl} = 21$ constraints. The mass profile model is described by $N + 1 = 12$ profile parameters and additional four calibration parameters ($\boldsymbol{c}$) to marginalize over.

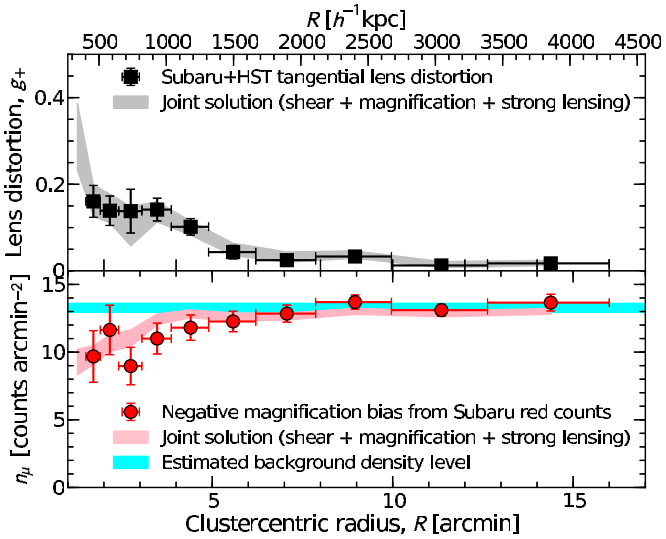

Figure 8. Top: tangential reduced shear profile $g_+(\theta)$ (squares) based on *HST* and Subaru distortion data of the composite full background sample. Bottom: coverage-corrected count profile $n(\theta)$ (circles) for a flux-limited sample of red background galaxies registered in the Subaru BR_cz' images. The horizontal bar represents the constraints on the unlensed count normalization, n_0, as estimated from Subaru data. Also shown in each panel is the joint Bayesian reconstruction (68% CL; solid area) from SL, WL tangential distortion (squares), and magnification-bias measurements (circles).

(A color version of this figure is available in the online journal.)

The resulting mass profile $\boldsymbol{s}$ from a joint SL+WL likelihood analysis of our *HST*+Subaru observations is shown in the top panel of Figure 9 (red squares; see also Figure 13, red squares). We find a consistent mass profile solution $\boldsymbol{s}$ as displayed in Figure 8 (solid areas). The projected cumulative mass profile $M_{\rm 2D}(<\theta)$ is shown in the lower panel (red curve). It is given by integrating the density profile $\boldsymbol{s} = \{\overline{\kappa}_{\infty,\rm min}, \kappa_{\infty,i}\}_{i=1}^{N}$ (see Appendices A and B of Umetsu et al. 2011a) as

$$M_{\rm 2D}(<\theta_i) = \pi(D_l\theta_{\rm min})^2\Sigma_{\rm crit}\overline{\kappa}_{\rm min} + 2\pi D_l^2\Sigma_{\rm crit} \times \int_{\theta_{\rm min}}^{\theta_i} d\ln\theta\,\theta^2\kappa(\theta). \quad (7)$$

The total projected mass enclosed within a radius of $\theta \approx 7' \approx 1.88\,{\rm Mpc}\,h^{-1}$ is found to be $M_{\rm 2D} = (3.1 \pm 0.5) \times 10^{15}\, M_\odot\, h^{-1}$.

As is evident from the cored density profile in the central region derived by SL, as well as from the flattened outer profile at large radii seen by WL (Figure 13), MACSJ0717 is a complex, non-relaxed cluster whose matter distribution is not well described by a single Navarro–Frenk–White (NFW, Navarro et al. 1996) profile. However, in order to derive a total (spherical) mass estimate of the main cluster component in a complementary (yet model-dependent) approach, we choose here to fit our full-lensing mass profile with a spherical NFW model.

To that end, the projected radial mass profile $\boldsymbol{s}$ is fitted with a model consisting of a halo component described by the two-parameter universal NFW profile, $\kappa_{\rm NFW}(\theta)$, and a constant mass-sheet component, κ_c:

$$\hat{\kappa}(\theta) = \kappa_{\rm NFW}(\theta) + \kappa_c, \quad (8)$$

where the constant κ_c approximates the inherent "two-halo" term contribution due to the clustering of halos (see Oguri & Hamana 2011). The NFW mass density profile is given by the form

$$\rho_{\rm NFW}(r) = \frac{\rho_s}{(r/r_s)(1+r/r_s)^2}, \quad (9)$$

Table 5
Best-fit NFW Parameters to Non-parametric Mass Reconstruction and Comparison with X-Ray and SZE Masses

Method	$R_{\rm vir}$ (Mpc h^{-1})	$M_{\rm vir}$ ($10^{15}\,M_\odot\,h^{-1}$)	$M(<500\,{\rm kpc}\,h^{-1})$ ($10^{15}\,M_\odot\,h^{-1}$)	κ_c[a]	$M_{\rm vir}/L_{R_C}$ ($h\,M_\odot/L_\odot$)	χ^2/dof[b]
1D WL+SL[c]	1.94 ± 0.14	$2.13^{+0.49}_{-0.44}$	0.63 ± 0.17	<0.01	301 ± 66	10/9
2D WL[d]	1.97 ± 0.15	$2.23^{+0.44}_{-0.38}$	0.54 ± 0.12	0.03 ± 0.01	310 ± 57	25/7
X-ray			$0.54^{+0.04}_{-0.08}$			
SZE			0.50 ± 0.04			

Notes.
[a] The constant dimensionless mass-sheet component.
[b] The goodness-of-fit, minimized χ^2 over number of dof.
[c] The NFW model was fitted to the mass profile fully reconstructed from WL+SL (see Section 7.1), constrained by 1D WL (shear+magnification)+SL Einstein-radius.
[d] The NFW model was fitted to the mass profile reconstructed from WL alone (see Section 7.2), using WL (2D shear+1D magnification), without SL constraints.

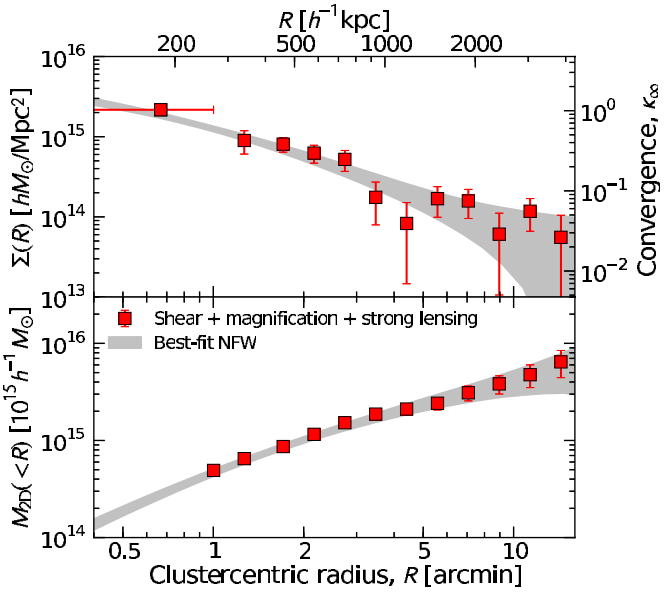

Figure 9. Top: surface mass density profile $\Sigma(R)$ (squares) derived from a joint SL, WL distortion and magnification (WL+SL) likelihood analysis of our *HST*+Subaru lensing observations. The gray area represents the best-fit NFW profile for the mass profile solution $\Sigma(R)$. Bottom: the cumulative mass $M_{\rm 2D}(<R)$ (red squares) as derived from the full lensing analysis. The gray area is the NFW fit (1σ confidence interval) to the WL+SL constraints as described above.

(A color version of this figure is available in the online journal.)

where ρ_s is the characteristic density, and r_s is the characteristic scale radius at which the logarithmic density slope is isothermal. The halo virial mass is then given by integrating the NFW profile (Equation (9)) out to the virial radius $r_{\rm vir}$, $M_{\rm vir} \equiv M(<r_{\rm vir})$. We specify the projected NFW model with the halo virial mass, $M_{\rm vir}$, and the degree of concentration, $c_{\rm vir} \equiv r_{\rm vir}/r_s$. We refer all of our virial quantities to an overdensity of $\Delta_c \equiv \Delta_{\rm vir} \approx 138$ based on the spherical collapse model using the fitting formula by Kitayama & Suto (1996, their Appendix A).[32]

We constrain the model parameters $\boldsymbol{p} = (M_{\rm vir}, c_{\rm vir}, \kappa_c)$ with our full-lensing mass profile $\boldsymbol{s}$. The χ^2 function for our SL+WL observations is[33]

$$\chi^2(\boldsymbol{p}) = \sum_{i,j}[\boldsymbol{s}_i - \hat{\boldsymbol{s}}_i(\boldsymbol{p})]C^{-1}_{ij}[\boldsymbol{s}_j - \hat{\boldsymbol{s}}_j(\boldsymbol{p})], \qquad (10)$$

where $\hat{\boldsymbol{s}}_i$ is the model prediction for the convergence profile $\boldsymbol{s}_i$ at θ_i and C is the full covariance matrix of $\boldsymbol{s}$ defined as $C = C + C_{\rm lss}$, with $C_{\rm lss}$ being the cosmic covariance matrix responsible for the uncorrelated LSS projected along the line of sight. For details, see Umetsu et al. (2011b).

Our best-fit NFW model to the combined lensing constraints (Equation (10)) is shown in Figure 9 as the gray shaded area. To summarize our results from this analysis, we obtain a total virial mass estimate of $M_{\rm vir} = (2.13^{+0.49}_{-0.44}) \times 10^{15}\,M_\odot\,h^{-1} \sim (3 \pm 0.6) \times 10^{15}\,M_\odot$ with the minimized χ^2 of 10 for 9 dof (see a summary in Table 5). We will compare and discuss all of the mass estimates yielded by the different modeling and reconstruction methods explored in the paper in Section 9.1.

At larger radii, a flattening of the mass profile is observed, possibly indicative of the surrounding LSS. The deviation of the profile from a single spherical NFW halo at large radius is indicative of substructure associated with this cluster region, and therefore merits a more careful 2D analysis, which we present in the next sections.

7.2. Mass Profile Reconstruction Using Two-dimensional Shear and Magnification

We follow Umetsu et al. (2012) to extend the one-dimensional (1D) Bayesian method above (Section 7.1) into a 2D mass distribution by combining the spatial shear pattern $(g_1(\boldsymbol{\theta}), g_2(\boldsymbol{\theta}))$ with the azimuthally averaged magnification measurements $n_\mu(\theta)$ (Section 4.2), imposing a set of azimuthally integrated constraints on the underlying $\kappa(\boldsymbol{\theta})$ field.[34] For details of the method, we refer the reader to Umetsu et al. (2012, their Appendix A.2).

By combining complementary WL distortion and magnification data in a non-parametric manner, we construct a 2D mass

[32] $\Delta_{\rm vir} \approx 140$ using the fitting formula by Bryan & Norman (1998).

[33] The calibration uncertainties in observational parameters, such as the background mean depths, $\langle\beta({\rm back})\rangle$ (or $z_{s,{\rm eff}}$) and $\langle\beta({\rm red})\rangle$, have already been marginalized over in the Bayesian mass profile reconstruction.

[34] Since the degree of magnification is locally related to κ, this will essentially provide the otherwise unconstrained normalization of $\kappa(\boldsymbol{\theta})$ over a set of concentric annuli where count measurements are available. We note that no assumption is made of azimuthal symmetry or isotropy of the cluster mass distribution.

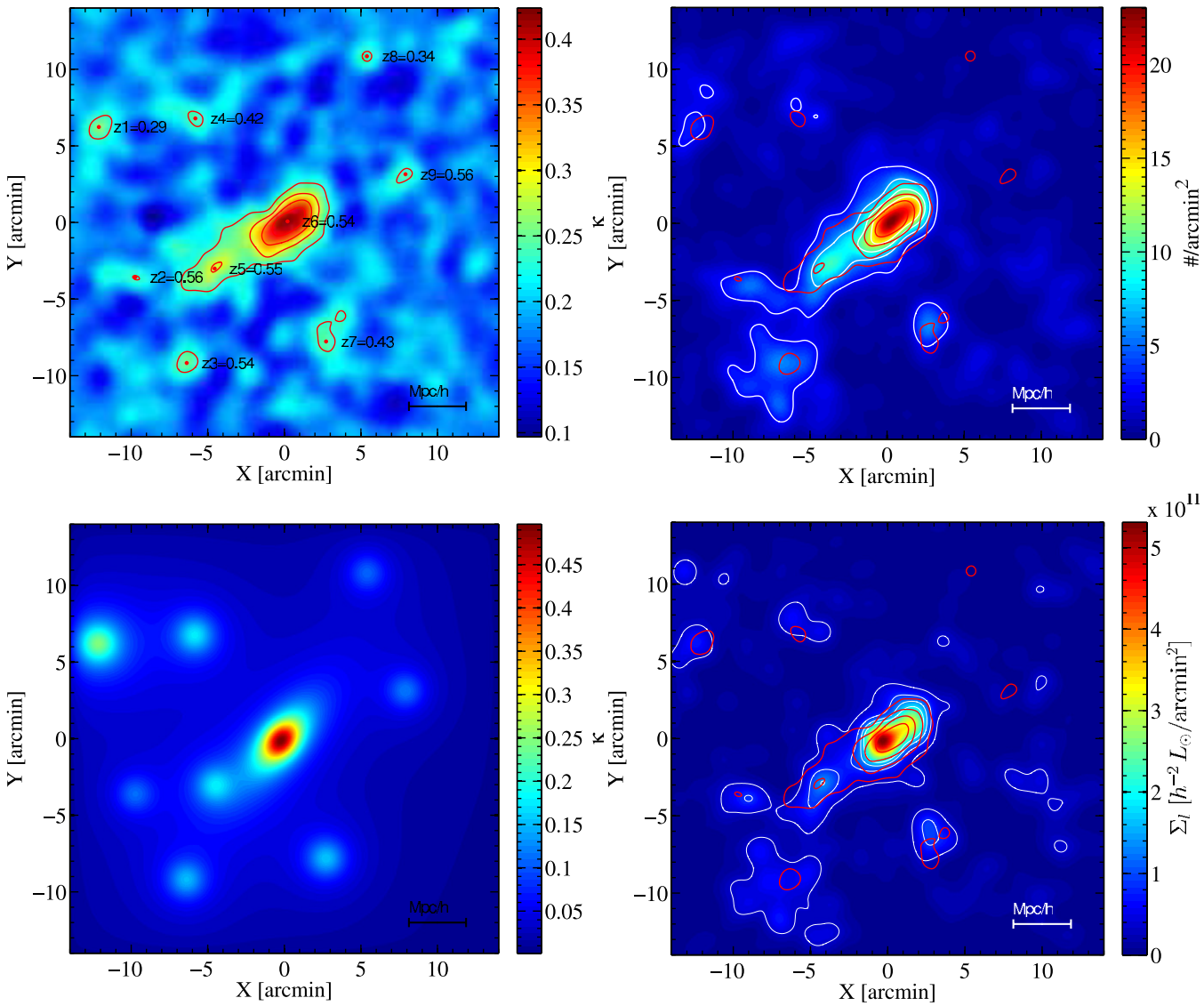

Figure 10. Top left: linear reconstruction of the dimensionless surface-mass density distribution, or the lensing convergence $\kappa(\boldsymbol{\theta}) = \Sigma(\boldsymbol{\theta})/\Sigma_{\rm crit}$, reconstructed from Subaru distortion data. The lowest red contour represents our detection level at $2.5\sigma_\kappa$, with further increments of $2\sigma_\kappa$. The red points denote the locations of the nine significant mass peaks identified above $2.5\sigma_\kappa$. Top right: surface number density distribution $\Sigma_n(\boldsymbol{\theta})$ of green galaxies, representing cluster member galaxies. White contours show $5\sigma_n$ increments starting at $2.5\sigma_n$. Also overlaid are the red contours of the convergence, showing very good agreement between the DM and the galaxy distributions. Bottom left: dimensionless surface-mass density distribution reconstructed from the multi-halo shear-fitting analysis, comprising the NFW halos fitted to the nine main mass peaks detected in Figure 10. The most massive central component was fitted by an elliptical-NFW model, whereas the other peaks are fitted by a simple NFW model. The parameters of each halo fit are given in Table 5. Bottom right: luminosity density distribution $\Sigma_l(\boldsymbol{\theta})$ of green galaxies, representing cluster member galaxies. The white contours show $5\sigma_l$ increments starting $2.5\sigma_l$ in number density. Also overlaid are the red contours of the convergence.

(A color version of this figure is available in the online journal.)

map over a 48×48 grid with $0.'5$ spacing covering the central $24' \times 24'$ field.[35] We show in Figure 13 (black circles) the azimuthally averaged radial mass profile $\Sigma(R)$ produced from the resulting mass map, given in 10 linearly spaced radial bins spanning from $\theta = 1.'5$ to $16'$. The innermost bin with the horizontal bar represents the mean interior mass density $\overline{\Sigma}(<1.'5)$ as marked at the area-weighted center $\overline{\theta} = 1'$. We find a model-independent constraint on the total enclosed mass within $\theta \approx 7'$ to be $M_{\rm 2D} = (3.4 \pm 0.6) \times 10^{15}\, M_\odot\, h^{-1}$.

We fit an NFW + mass-sheet model (Equation (8)) to the WL radial mass profile derived here by minimizing the total χ^2 function defined as in Equation (10), marginalizing over the mean background depth uncertainty in $z_{s,\rm eff}$. We find the total virial mass to be $M_{\rm vir} = (2.23^{+0.44}_{-0.38}) \times 10^{15}\, M_\odot\, h^{-1}$. We summarize all of the results from our analyses in Table 5 and discuss the differences in Section 9.1.

[35] The magnification analysis is limited within the central $24' \times 24'$ region where the number counts of red background galaxies are reliably measured.

8. SPATIAL MASS DISTRIBUTION ANALYSIS

Here we present the full 2D mass distribution in the cluster and its surrounding structures as constrained by WL shear in Section 8.1, and we further constrain the mass of the individual components by modeling identified halos independently in Section 8.2. We present another 2D inversion method, SawLenS, in Section 8.3, which incorporates information from WL shear and SL on a multi-scale grid. Finally, we probe the substructure in the core of the cluster in Section 8.4.

8.1. Mass and Light Distributions of the Cluster and Surrounding Large-scale Structure

WL distortion measurements (g) can be used to recover the underlying projected mass density field $\Sigma(\boldsymbol{\theta})$. Here we use the linear map-making method outlined in Section 4.4 of Umetsu et al. (2009) to derive the projected mass distribution from the *HST*+Subaru distortion data presented in the previous sections.

In Figure 10 (top left panel), we show the surface-density field $\kappa(\boldsymbol{\theta})$ in the central $28' \times 28'$ region, reconstructed from the background (blue+red) sample (Section 3.2), where, for visualization purposes, the mass map is smoothed with a Gaussian of $\theta_{\rm FWHM} = 1.'5$. We overlay the mass map with contours starting at $2.5\sigma_\kappa$ above the background, which is equivalent to a detection threshold of $\Sigma_{2.5\sigma_\kappa} = 3.66 \times 10^{14}\, h\, M_\odot\, {\rm Mpc}^{-2}$, and separated by $2\sigma_\kappa$ intervals.

A very elongated structure is evident, and several mass clumps seem to comprise the cluster. Some clumps lie outside of the estimated virial radius which is at $\sim$2 Mpc h^{-1}. Some of these mass structures may in fact lie in the foreground of the cluster and not be physically associated with it, yet contribute to the overall lensing of the background galaxies. Therefore, we need to estimate the mean redshift of each of these significant structures.

In order to estimate the distances to the detected structures, and to correlate the galaxy distribution in this cluster and its surrounding structure with the DM distribution, we utilize the green sample defined in Section 3.1, which comprises mostly cluster galaxies and some lower-level contamination of foreground galaxies. We construct both a 2D galaxy number-density map (Figure 10, top right panel) and a K-corrected $R_{\rm C}$-band luminosity density map (Figure 10, bottom right panel). Both maps are smoothed with a Gaussian of the same scale as the mass map above, $\theta_{\rm FWHM} = 1.'5$. The white contours are overlaid with 5σ increments starting at 2.5σ above the background level of the equivalent map. We also overlay the surface mass density map (red contours) as determined above to illustrate the correlation.

Overall, the DM distribution is well traced by the galaxy distribution, as evident by the overlapping contours and the proximity of the mass peaks to the light peaks. The good agreement seen is consistent with the smaller mass halos being in the process of accreting onto the main halo. A further detailed analysis of individual structures is presented below (Section 8.2).

8.2. Multi-halo Mass Reconstruction

To estimate individual masses of the structures comprising the cluster and its surroundings as seen within the scope of the Subaru, $\sim$0.25 deg^2, we now present a multi-halo fitting approach. We first identify the most dominant peaks from the convergence map presented above (Section 8.1, Figure 10). These are defined as all peaks lying $2.5\sigma_\kappa$ above the background level, estimated from a bi-weighted scale and mean (Beers et al. 1990), respectively, outside the region of $8'$ from the cluster center, so as not to be biased by the cluster potential. The $2.5\sigma_\kappa$ detection level is indicated as the first red contour in Figure 10, corresponding to $\Sigma_{2.5\sigma} = 3.66 \times 10^{14}\, h\, M_\odot\, {\rm Mpc}^{-2}$.

We have detected nine distinct mass peaks, numbered z_1–z_9 in Figure 10 (top left, the peak locations are marked with red points) and in Table 5. To help identify whether these peaks are part of the same structure as the cluster or unassociated systems projected along the line of sight, we estimate the photometric redshift of each component. For this we take the mean photometric redshift of matching member galaxies in the green sample (Section 3.1) lying within $1'$ from the respective mass halo peak. As evident, only five of the nine structures lie at approximately the same redshift (z_2, z_3, z_5, z_6, z_9) as that of the cluster, whereas the other mass clumps lie at $z_1 = 0.29$, $z_4 = 0.42$, $z_7 = 0.43$, and $z_8 = 0.34$ in the foreground of the cluster.

We then perform a 2D shear analysis to constrain the mass properties of the cluster and its surrounding structure, modeled as the sum of nine mass halos in projection space. The multi-halo shear modeling procedure described here is similar to those of Watanabe et al. (2011), Okabe et al. (2011), and Zitrin et al. (2012a), but including an elliptical halo model as described below. More details will be presented in our forthcoming paper (K. Umetsu et al. 2013, in preparation).

First, we construct a reduced-shear map ($g_1(\boldsymbol{\theta})$, $g_2(\boldsymbol{\theta})$) on a regular grid of $N_{\rm cell} = 42 \times 42$ independent cells, covering a $28' \times 28'$ region centered on the cluster. We exclude from our analysis those cells lying within $1.'5$ from the cluster center and those lying within $0.'5$ from the other less-massive halo peaks, to avoid potential systematic errors due to contamination by unlensed cluster member galaxies (Section 3). This leaves us with a total of 1813 usable measurement cells, corresponding to 3626 constraints.

We describe the primary mass peak, responsible for the main cluster, as an elliptical NFW (eNFW, hereafter) model specified with six parameters, namely, the halo virial mass ($M_{\rm vir}$), concentration ($c_{\rm vir}$), ellipticity ($e = 1 - b/a$), position angle of the major axis (θ_e), and centroid position (X_c, Y_c). We introduce the mass ellipticity e in the isodensity contours of the projected NFW profile $\Sigma(X, Y)$ as $R^2 = (X-X_c)^2+(Y-Y_c)^2 \rightarrow (X - X_c)^2(1 - e) + (Y - Y_c)^2/(1 - e)$ (see Oguri et al. 2010; Umetsu et al. 2012). For each of the other eight less massive halos, we assign a spherical NFW profile parameterized with the virial mass ($M_{\rm vir}$), where the centroid position is fixed at the respective mass peak location. Since these less massive halos are less resolved by our WL observations, their concentration parameters are set according to the mass–concentration relation $c_{\rm vir}(M_{\rm vir}, z)$ given by Duffy et al. (2008).

We use the MCMC technique with Metropolis–Hastings sampling to constrain the multi-halo lens model from a simultaneous nine-component fitting to the reduced-shear map. The best-fit parameters are reported in Table 5. We find virial masses of $M_{\rm vir} = (1.71 \pm 0.26) \times 10^{15}\, M_\odot\, h^{-1}$ for the main cluster halo, z_6, and masses of $M_{\rm vir} = (0.15 \pm 0.09)$, (0.27 ± 0.11), (0.25 ± 0.11), and $(0.19 \pm 0.10) \times 10^{15}\, M_\odot\, h^{-1}$ for the other smaller halos, z_2, z_3, z_5, z_9, respectively, that lie at the same redshift. The high value of the ellipticity, $e = 0.59 \pm 0.08$, inferred from our elliptical lens modeling (similar to the cases of, e.g., MACS J0416 by Zitrin et al. 2013; RX J0152.7-1357 by Jee et al. 2005 and Umetsu et al. 2005) supports that the central component of MACS0717 represents a merging, interacting system of multiple clumps in the process of formation (as shown in Ma et al. 2009; Mroczkowski et al. 2012).

Comparing the cluster luminosity and galaxy maps, most of the significant mass structures detected in the mass map are also probed by the galaxies, with the exception of two lower-significance structures, marked as z_8 and z_9. The mass structure z_8 is not evident in the galaxy density map, but can be explained by the existence of lower-redshift galaxies seen therein, $z_8 = 0.34$, which is close to the limit probed by our color-selection method (see Figure 3, green). The other mass structure, z_9, is not detected in the galaxy density map, however,

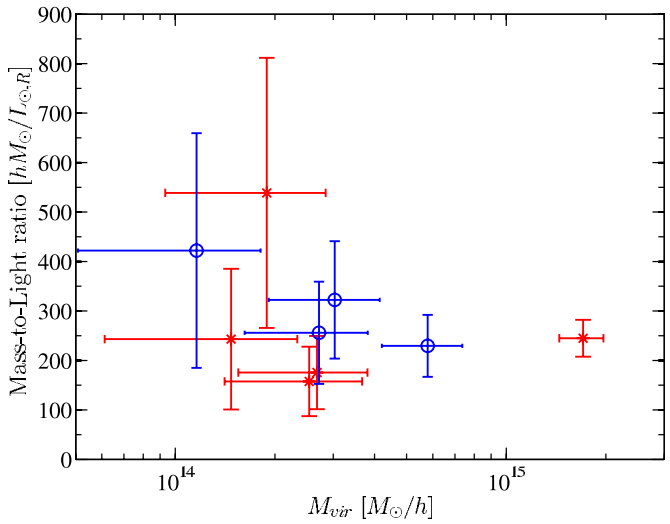

Figure 11. Mass-to-light M/L vs. $M_{\rm vir}$ for the nine halos modeled in Section 8.2. The mass halos that lie at the cluster redshift are shown as red stars, and the mass halos at the foreground of the cluster are plotted with blue circles. The first two points at $\sim 1 \times 10^{14}\ M_\odot\, h^{-1}$ correspond to the lower-significance halos that have no optical counterpart (see text).

(A color version of this figure is available in the online journal.)

a low-significance peak is seen (more evident in the luminosity map) offset by $\sim$1.′5 to the north-east, where visual inspection reveals a BCG, albeit also at $z \approx 0.34$, therefore not part of the cluster structure. A $\sim$1.′5 offset is comparable to our smoothing scale, therefore within errors.

To further determine if the detected and modeled halos are real, and if their content represents the typical stellar content of cluster-sized halos, we calculate the mass-to-light (M/L) ratio of the individual halos modeled. We divide the fitted virial mass of each halo, $M_{{\rm vir},i}$, by the total luminosity of "green" galaxies within the equivalent virial radius of the halo (virial ellipse in the case of the main halo modeled with eNFW, z_6), $L_i = \sum_{k \in r < r_{{\rm vir},i}} L_{R{\rm C},k}$. We list the M/L ratios in Table 6, and we plot the resulting $M_{\rm vir}/L$ versus $M_{\rm vir}$ in Figure 11. All of the halos, apart from halos z_8 and z_9 discussed above, show values that are expected for group- to cluster-sized halos, ranging from $\approx$200–300 (Rines et al. 2000, 2004; Katgert et al. 2004). However, the large uncertainties in the M/L ratios measured, especially for the low-mass halos, limit us from determining if there is any trend in this relation.

For a consistency check, we also calculate the M/L ratios for the single-halo NFW models we fit to our reconstructed mass profiles in Sections 7.1 and 7.2 (listed in Table 5), and compare with the M/L ratio we get for the main halo from our multi-halo modeling, $M/L_6 \sim 245$. Within the errors, we get comparable M/L values for the 1D NFW fit (Sections 7.1), $M/L \sim 300$, which are reasonable for a cluster as massive as MACSJ0717, whereas the values for the NFW fit to the 2D mass reconstruction method given in Section 7.2, $M/L \sim 310$, are only slightly higher, reflecting the higher total mass found, due to the inclusion of the second massive halo at larger radii in the virial mass fitted.

8.3. SaWLens SL+WL Reconstruction

We perform a complementary joint SL+WL reconstruction using the method of Merten et al. (2009, 2011, hereafter SaWLens). The SaWLens method combines central SL constraints from multiple-image systems with WL distortion constraints in a non-parametric manner to reconstruct the underlying lensing potential on a multi-scale grid. Here, the density of constraints sets our resolution scale. Inside the *HST* region, we combine constraints from *HST* WL shape distortions with those of SL multiple-image sets. This yields a very high-resolution scale of 9″ box size. Beyond this, we rely on Subaru WL shape distortion constraints, yielding a resolution scale of 25″. There is good consistency between the mass structures probed by the mass map derived here and in Section 8.1. We further derive an azimuthally averaged mass profile in order to compare with our other mass profiles derived with the methods presented in the previous sections (see Figure 13, blue triangles). SaWLens error bars were derived from 1000 bootstrap realizations of the WL input catalog and from 2000 resamplings of the SL input data. Since many of the multiple image systems have only (less certain) photometric redshifts as derived from *HST* imaging, SL realizations were obtained by randomly assigning redshifts within the equivalent uncertainties of each system. We further present the inner substructure seen by this method in the next subsection.

8.4. Mass and Light Distribution inside the Cluster Core

In this subsection, we present the 2D analysis of the WL shear map as measured from background galaxies in the *HST* field, defined in Section 6. We also present the inner region of the SaWLens reconstruction as an independent analysis of the cluster core.

To avoid systematic effects due to the finite-field of the *HST* FOV, we combine our *HST* background sample with the Subaru background sample (Section 6), where we remove Subaru objects that match with *HST* objects to avoid duplication. We also correct for the different depths of the *HST* relative to the Subaru background samples, as explained in Section 6. In order to avoid infinite noise issues, we first smooth the 2D shear field with a Gaussian of 0.′25 FWHM. This essentially limits our sensitivity to mass structure at small angular scales, depending on the local source number density (S/N $\propto n_g^{1/2}$).

We reconstruct the high-resolution mass map in the central $5' \times 5'$ region from the 2D shear map, using an entropy-regularized maximum-likelihood reconstruction method (hereafter, maximum entropy method, or MEM) of Umetsu & Broadhurst (2008). We present the resulting mass distribution in Figure 12 (upper left) in terms of the reconstruction S/N map, with 3, 5, 7σ_κ mass contours overlaid. The errors for the mass map are based on the theoretical covariance matrix (Umetsu & Broadhurst 2008). As an independent comparison, we also present the inner region of the mass map derived from the SaWLens method, described in the previous section. This is shown in Figure 12 (right panel). A grid-size of $\sim$9″ is possible in this region due to several SL multiple-image systems, augmented by the *HST* measured WL galaxy shapes. We overlay the light distribution in both maps (white contours) as determined from the cluster members selected in Section 6.

Broadly, both maps show a mass distribution that follows the light as determined by the member galaxies. Substantial substructure is probed by both methods, and several distinct mass peaks are evident throughout. The complexity of the mass distribution demonstrates that a clear center is not well-defined in this cluster, which instead of a dominant BCG has several bright galaxies associated with the different mass clumps. This level of substructure was previously reported by Ma et al. (2009) from *Chandra* X-ray data, showing several brightness peaks (see their Figure 1) and an extended shock feature. We overlay

Table 6
Best-fit NFW Multi-halo Parameters of the 2D Shear Analysis

Halo	ΔX[a] (arcmin)	ΔY[a] (arcmin)	z_l[b]	z_s[c]	$R_{\rm vir}$ (Mpc h^{-1})	$M_{\rm vir}$[d] ($10^{15}\,M_\odot\,h^{-1}$)	e[e]	θ_e[f] (deg)	$M_{\rm vir}/L_{R_C}$ ($h\,M_\odot/L_\odot$)
z1	-12.11	6.23	0.29	1.21	1.45	0.58 ± 0.16	...	...	230 ± 63
z2	-9.73	-3.57	0.56	1.27	0.79	0.15 ± 0.09	...	...	243 ± 142
z3	-6.37	-9.17	0.54	1.26	0.97	0.27 ± 0.11	...	...	176 ± 74
z4	-5.81	6.79	0.42	1.24	1.09	0.30 ± 0.11	...	...	322 ± 119
z5	-4.55	-3.01	0.55	1.26	0.95	0.25 ± 0.11	...	...	158 ± 70
z6	-0.21 ± 0.06	-0.09 ± 0.07	0.54	1.26	1.81	1.71 ± 0.26	0.59 ± 0.08	50 ± 5	245 ± 37
z7	2.73	-7.77	0.43	1.24	1.04	0.27 ± 0.11	...	...	256 ± 103
z8	5.39	10.85	0.34	1.22	0.82	0.12 ± 0.07	...	...	422 ± 237
z9	7.91	3.15	0.56	1.27	0.86	0.19 ± 0.10	...	...	539 ± 273

Notes. For the main cluster component (z_6), the halo centroid was allowed to vary, and an eNFW model was fitted. The concentration parameter was also fitted here, whereas for all other less massive halos the concentration was set by the mass–concentration relation given by Duffy et al. (2008).
[a] The centroid position of each halo is given relative to the cluster center (see Table 1) in units of arcminutes.
[b] The median photometric redshift for each halo estimated from the green sample.
[c] The photometric source redshift for each halo. In the multi-halo shear fitting process, we assumed a flat prior over the range $z_s \pm 0.1$.
[d] Marginalized bi-weight center and scale locations are reported.
[e] The projected mass ellipticity of our eNFW model is defined as $e = 1 - b/a < 1$ with a and b the major and minor axes of the isodensity contours.
[f] The position angle of the eNFW halo major axis is given in units of degrees, measured north of west.

the X-ray map (also rederived here in Section 9.2 below) on the *HST* color image (Figure 12, bottom right). Combining with dynamical measurements, Ma et al. (2009) concluded the existence of four main mass halos (denoted A, B, C, and D in their figure) suggesting a triple-merger. One of those clumps (B) was shown to still be in its infancy at a very high collision velocity of $s \sim 3000$ km s^{-1}, infalling through the cluster. Using their SL model, L12 also find a similar substructure in the DM distribution, and attempt to model the mass map with 1–5 mass halos, finding a best solution given by 4 mass halos. We note L12's peaks on both maps (blue crosses, denoted as A–D following Ma et al.'s designation).

We also overlay the MEM mass contours on the SL model derived in Section 5, shown along with L12 mass peak locations in the bottom-right panel of Figure 12. We note that the WL–MEM results agree very well with our parametric SL results (Section 5), both demonstrating an overall agreement between the distributions of the galaxies and DM, although our parametric SL method does use the light distribution as an initial approximation of the mass. For the WL–MEM results, this is not trivial at all, because the WL–MEM method is entirely non-parametric and is not aware of the distribution of cluster members, hence providing a model-independent reconstruction of the underlying total mass distribution.

Although we find an overall agreement with previous and current SL analyses where the DM follows the location of the galaxies, some differences are noticeable. From the MEM-derived mass map, the peak location of the main clump "C" is somewhat offset from those of cluster galaxies and X-ray emission (that rather agree with each other) by about $\sim 0\farcm33 \approx 90$ kpc h^{-1}, although their extended features overlap well with each other.

The SaWLens derived map, on the other hand, shows much larger differences between the mass and light distributions. The mass peaks in the SaWLens reconstruction are mostly offset from those of cluster galaxies. Most notably, the location of the SaWLens mass peak nearest to clump "A" is further displaced to the center than the light or the location found by L12, and clump "B" is much less pronounced in this mass map.

The current analysis is limited by the spatial resolution set by the number density of background galaxies, and may be prone to potential systematics, especially in the critical lensing regime. Therefore, in this work, we cannot draw any significant conclusion about the level of offsets between the DM, galaxies, and hot gas.

9. DISCUSSION

9.1. Mass Profiles from Different Lensing Methods

The mass profiles we constructed in the previous sections using various methods are summarized in Figure 13: a parametric light-traces-mass SL mass profile (green; Section 5), a non-parametric Bayesian mass profile incorporating WL 1D shear+magnification constraints and the SL mass constraint (red squares; Section 7.1), a non-parametric approach combining WL 2D shear+ 1D magnification constraints (black circles; Section 7.2), and finally, a mass profile obtained with SaWLens (blue triangles; Section 8.3), an independent non-parametric reconstruction combining SL+WL shear constraints on a joint multi-scale grid. Here we summarize and compare the different results.

As can be seen, overall good agreement is found in the regions of overlap between the different reconstruction methods, within the errorbars. The relatively good agreement we find on large scales is reassuring, given that it is all based on the same Subaru imaging data. At $r > 1$ Mpc h^{-1}, there is general change in the sign of the gradient of the mass profile, where a clear flattening tendency is seen. A similar behavior was also found in our recent CLASH lensing analysis of the high-mass relaxed cluster MACSJ 1206-08 at $z = 0.44$ ($M_{\rm vir} \simeq 1.1 \times 10^{15}\,M_\odot\,h^{-1}$; Umetsu et al. 2012), albeit to a lower extent, and may in both cases reflect the relative prominence of the surrounding filamentary pattern of structures extending beyond the virial radius, and hence the relatively less evolved stage of these very massive clusters at $z \sim 0.5$ compared to their lower redshift counterparts, such as A1689 and A1703, where the outer mass profile continues to steepen (Broadhurst et al. 2005b; Umetsu et al. 2011a) and for which no prominent filamentary network is visible.

MACSJ0717 has recently been analyzed by Jauzac et al. (2012) using multiple *HST*/ACS pointings aimed at covering the filamentary structure around the cluster. Their mass

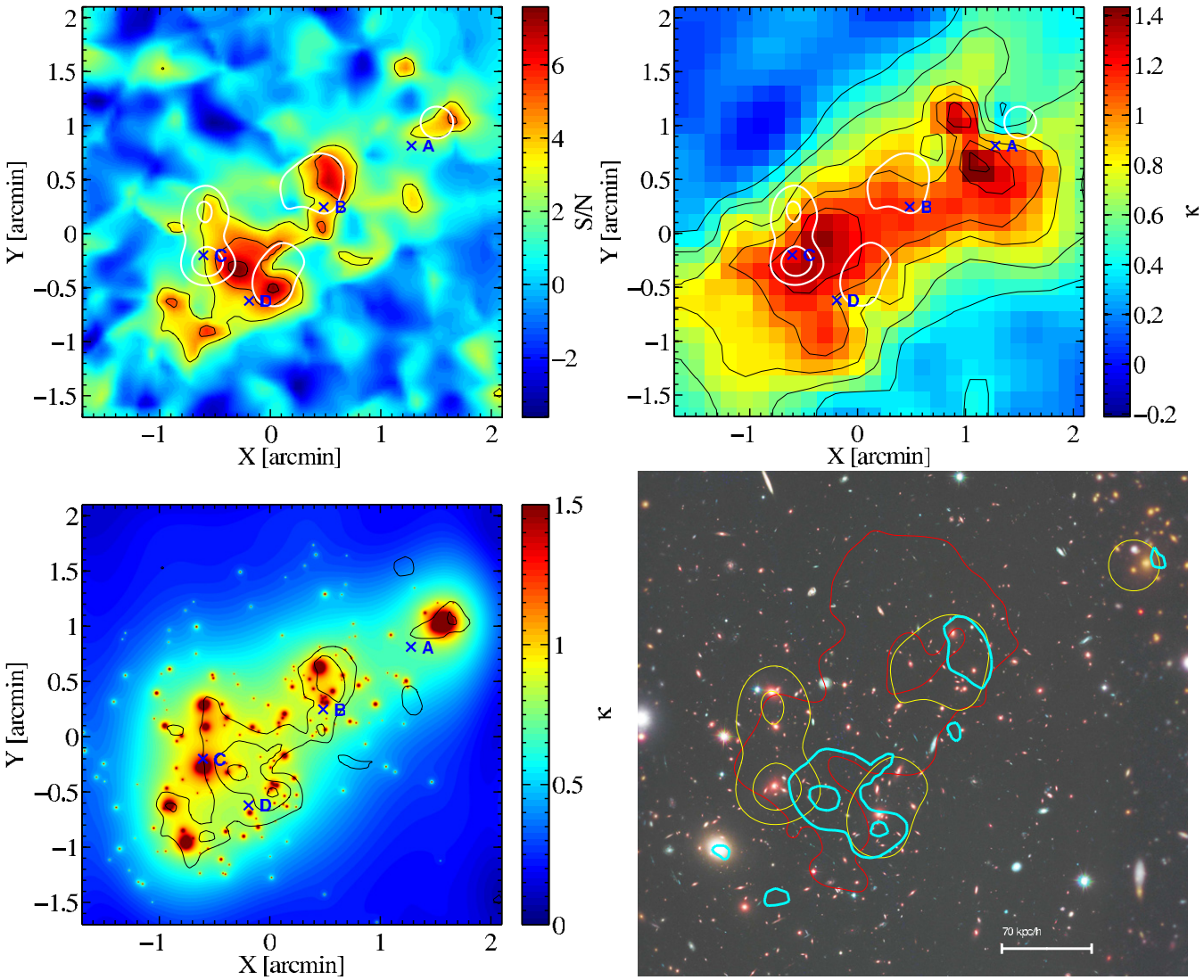

Figure 12. Top left: S/N map of the WL MEM reconstructed mass-density distribution. The black contours start at $3\sigma_\kappa$ with $2\sigma_\kappa$ intervals. We also plot the light contours (white), and the SL mass peak (A–D) found by L12. Top right: the SaWLens SL+WL reconstructed mass-density distribution, light contours (white), and L12 SL mass peak. Bottom left: the parametric SL model derived in Section 5, using the light from cluster galaxies as a proxy of the mass. The WL MEM mass reconstruction (black contours) and L12 SL mass peaks are also overlaid. Bottom right: *HST* color image of MACSJ0717. The cyan contours show the DM distribution as determined from the WL shear analysis. The yellow contours show the light distribution of cluster members. The red contours show the *Chandra* X-ray luminosity map. The cluster DM component is comprised of several mass clumps, with several offsets between the DM, gas, and galaxies. Notably, the central DM core lies between the light peaks.

(A color version of this figure is available in the online journal.)

reconstruction shows slightly higher densities at all radii and most notably at the outer radii, albeit still in agreement with our 2D shear+magnification density profile (black circles), within the errors. This small systematic difference may arise due to Jauzac et al.'s strategy of surveying only the area where the filamentary structure is dominant, so that the mean lensing signal that we obtain with our larger FOV is on average expected to be lower, as observed.

The total masses of the cluster are presented in Section 9.4 where we compare with prediction for the highest mass halos expected in the context of the ΛCDM model.

9.2. X-Ray Results from Chandra and XMM-Newton

Here we compare complementary X-ray derived total masses to our 1D lensing-derived total masses. One mass estimator uses the assumption that the gas fraction at r_{2500} is constant (for this work we assume $f_{\rm gas} \equiv M_{\rm gas}/M_{\rm total} = 0.11$). The other common mass estimator uses the assumption that the primary pressure support for the gas is thermal pressure, that is, that the gas is in nearly hydrostatic equilibrium (HSE). While it is true that this system is merging and highly complex (as shown in Ma et al. 2009), a comparison of the HSE mass with the lensing mass can be used to place estimates on the magnitude of non-thermal pressure support in the gas, such as bulk motions and turbulence.

We analyze public *Chandra* observations from a single OBS-ID (4200) with a net exposure time of 59,000 s. Gas density profiles from the ACCEPT database (Cavagnolo et al. 2008) were used to generate an enclosed gas mass profile. We also derived radial profiles based on spectra extracted from concentric annular apertures. The tool used for the HSE mass estimate is Joint Analysis of Cluster Observations (JACO; Mahdavi et al. 2007, we refer the reader to this paper for the details of the X-ray analysis procedure). The best-fit NFW parameters derived from the joint JACO fit at r_{2500} are

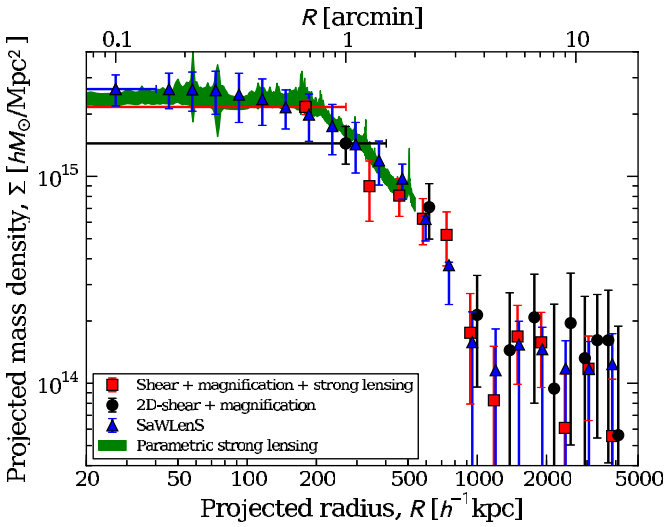

Figure 13. Surface mass density profile, combining and comparing results from our parametric SL analysis of CLASH-*HST* data (green), 1D WL (shear+magnification) + SL analysis (red squares), 2D WL (shear+magnification) analysis (black circles), and SaWLens 2D shear+SL analysis (blue triangles). All the WL-shear analyses are based on both *HST* and Subaru datasets, where the WL constraints at $\gtrsim 3'$ are based on the Subaru observations. Good agreement between the SL and WL analysis is seen in the region of overlap. There is also good agreement between the different methods of WL analysis.

(A color version of this figure is available in the online journal.)

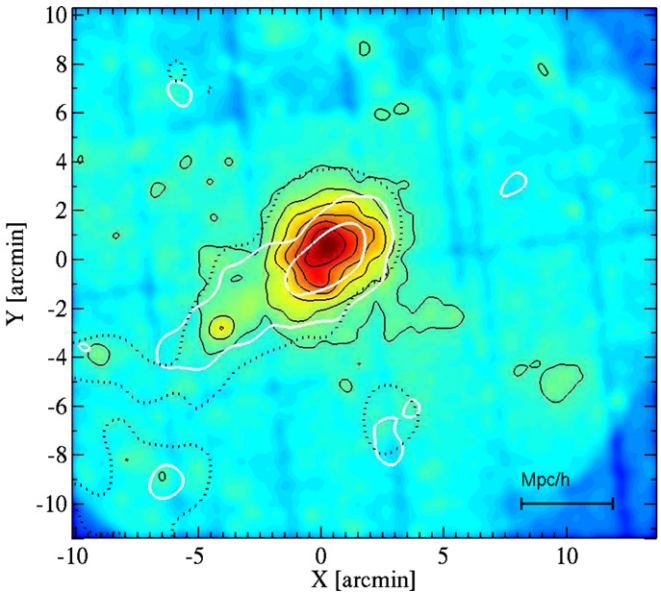

Figure 14. X-ray map from *XMM-Newton* data in logarithmic scale, smoothed to $\theta_{\rm FWHM} = 0.'5$, with 1.5σ contours with 2σ intervals (solid black lines). Also overlaid are κ contours (solid white lines) and galaxy density contour (dotted black line).

(A color version of this figure is available in the online journal.)

$M_{2500} = 4.45^{+0.95}_{-0.46} \times 10^{14}\, M_\odot\, h^{-1}$, $c_{2500} = 0.6 \pm 0.3$. The X-ray profile has a limited range $r < 0.7\,{\rm Mpc}\,h^{-1}$.

We compare the X-ray total mass within $r < 500\,{\rm kpc}\,h^{-1}$ with lensing-derived values at the same clustercentric radius in Table 5. The X-ray mass seems to be about ∼87% of the lensing 1D WL+SL NFW fitted value. In Figure 15, we compare the resulting total mass ($M_{\rm 3D} < r$) profiles from the X-ray fit (magenta) and the lensing 1D WL+RE NFW fit (orange). We find that the X-ray mass profile derived with the HSE assumption underestimates the lensing profile at all radii. The difference is most extreme in the core of the cluster, where the HSE X-ray mass is only 45% of the WL mass, rising to agreement with the WL mass at the limit of the X-ray data, $r = 0.7\,{\rm Mpc}\,h^{-1}$. This inconsistency clearly stems from the departure from HSE at the center of the cluster where significant merging activity has been claimed, augmented by the highly non-spherical shape of the cluster (Meneghetti et al. 2010; Rasia et al. 2012). We enhance our discussion below by further comparing to the SZE-derived mass (see Section 9.3) which also relies on the HSE assumption.

For a wider look at the 2D distribution of the gas, we also analyze *XMM-Newton* observations of MACSJ0717 recently made public (P.I. Million, observations 672420101, 672420201, 672420301, totaling 145,000 s). We perform a standard reduction on the observations, removing high flare times. To achieve the best sensitivity to gas at large clustercentric radius, we summed the MOS1, MOS2, and *p–n* CCDs of all three observation sets. The brightest point sources were identified and excluded. Since the PSF for *XMM* gets fairly distorted and elongated at off-axis angles, there is incomplete removal of the halos around point sources there.

We present the logarithmic X-ray brightness map in Figure 14, where we smooth the map with a Gaussian of $\theta_{\rm FWHM} = 0.'5$ and overlay it with logarithmic contours starting at $1.5\sigma_X$ above the background with $2\sigma_X$ intervals (solid black lines). For comparison, we overlay the mass density (2.5- and 6.5-σ_κ) contours from the Subaru lensing map (solid white line) and the galaxy distribution $2.5\sigma_n$ contour (dotted black line).

The cluster X-ray brightness peak is clearly shifted from the mass (and galaxy) peak, at about $R = 0.'37 = 100\,{\rm kpc}\,h^{-1}$ north-west of the optical center. This has been noted in previous detailed analyses of the cluster center (Ma et al. 2009) and was interpreted to be due to trailing of the gas component behind the cluster as subclumps cross through the main cluster halo, because the gas and the DM have different cross-sections. In Table 1, we summarize the location of the optical center we have been using and that of the X-ray brightness peak.

With the advent of the *XMM-Newton* data, we can also see here the clear detection of the secondary massive component (denoted z_5 in our mass map, see Figure 10) at a $5.5\sigma_X$ level, and the third mass component (denoted z_2 in our mass map) at a $2.5\sigma_X$ level. Finally, the fourth mass component detected from lensing, z_3, is evident in the map but at a much lower significance, $\sim 1.6\sigma_X$. Although lensing shows this halo to be more massive than z_2, it is hard to detect it in the X-ray image since it lies at the edge of our data where it is more prone to contamination by point sources.

Overall, it seems the gas in the outskirts (at a scale of $\lesssim 0.7\,{\rm Mpc}\,h^{-1}$) is more spherically distributed around the main cluster component, but has the same substructure corresponding to high-mass peaks along the filamentary structure. The emission from the hot gas is expected to be more spherical in shape than that mapped by lensing because the gas in projection traces the gravitational potential, which is rounder than the density distribution.

9.3. SZE Results Using Bolocam

We obtained SZE observations of MACSJ0717 using Bolocam at the Caltech Submillimeter Observatory. Bolocam is a 144-element bolometric array operating at 140 GHz with an angular resolution of 58″ (FWHM). The data were collected by scanning Bolocam's 8′ FOV in a Lissajous pattern to produce an image with coverage extending to $\simeq 10'$ in radius. Full

details of the observations are given in Mroczkowski et al. (2012) and Sayers et al. (2013), and the data were reduced using the procedures described in Sayers et al. (2011). In addition, we note that in the multiwavelength SZE analysis of Mroczkowski et al. (2012), which used the same Bolocam SZE data as this analysis, a tentative kinetic SZE signal from subclump "B" of Ma et al. (2009) is reported at a significance of $\simeq 2\sigma$. Consequently, we subtracted the best-fit kinetic SZE template of Mroczkowski et al. (2012) from our data, although we note that Mroczkowski et al. (2012) were not able to robustly constrain a spatial template of this kinetic SZE signal, modeling it as a simple Gaussian centered on the location of "B." We then fit a spherical generalized NFW (gNFW) pressure model (Nagai et al. 2007) to our SZE data allowing both the normalization and scale radius to vary while using the best-fit slope parameters found by Arnaud et al. (2010).

We compute the mass of MACSJ0717 from this gNFW fit to the SZE data using the formalism described by Mroczkowski (2011). In particular, we assume that the cluster is spherical and in HSE, although we note that neither of these assumptions are strictly valid for MACSJ0717 due to its complex dynamical state. The resulting SZE mass profile is shown in blue in Figure 15, and we note that it is approximately ∼75% of our lensing-derived mass profile. However, the SZE mass profile is in reasonably good agreement with the X-ray derived mass profile, which also assumed HSE. Therefore, we conclude that the difference is due to the bias associated with assuming HSE. For example, even for relaxed systems, we expect the HSE-derived virial mass to be biased approximately 10%–20% lower on-average compared to the true virial mass due mainly to bulk motions in the gas (Nagai et al. 2007; Rasia et al. 2004, 2012; Meneghetti et al. 2010). Furthermore, in order to gauge the impact of the kinetic SZE signal from subclump "B," we also computed an SZE mass profile without subtracting the kinetic SZE template (shown in gray in Figure 15). As expected, the difference between the two SZE mass profiles is most significant in the inner regions of MACSJ0717 near the center of subclump "B," where the corrected mass is ∼50% lower than the uncorrected one, decreasing to only $\lesssim$15% difference at large radius.

9.4. Total Mass Compared with ΛCDM Predictions

We have reliably estimated the total mass of the cluster in Sections 7.1 and 7.2 to be $M_{\rm vir}(1{\rm DWL+SL}) = 2.13 \times 10^{15}\,M_\odot\,h^{-1}$ and $M_{\rm vir}(2{\rm DWL}) = 2.23 \times 10^{15}\,M_\odot\,h^{-1}$, respectively, as summarized in Table 5. We note that the two masses are in excellent agreement. In Section 8.2, we derived specific masses for the individual halos comprising the cluster and its surrounding structures, in order to more accurately account for the LSS contribution to the mass. Here we use as the total mass for MACSJ0717 the sum of the virial masses of the two components that lie within the virial region of the main halo, $M_{\rm vir}(z_5+z_6) \approx (1.96 \pm 0.28) \times 10^{15}\,M_\odot\,h^{-1}$, as determined by multi-halo modeling (see Tables 6) which is slightly lower, but still consistent with the values found from single-halo modeling noted above.

Another total mass estimate for this cluster was previously presented in Hoekstra et al. (2012), part of a larger 50-cluster batch analysis. That measurement solely relied on WL shear measurement, and did not simultaneously constrain both $c_{\rm vir}$ and $M_{\rm vir}$, as done here, but relied on the Duffy et al. (2008) relation, which, according to their published mass of $M_{\rm vir} = 5 \times 10^{15}\,M_\odot\,h_{70}^{-1}$, should be $c_{\rm vir} = 3.05$. Forcing this concentration value, our mass would have been $M_{\rm vir} = (4.5 \pm 0.6) \times 10^{15}\,M_\odot\,h_{70}^{-1}$, consistent with their mass. Since there is a strong negative correlation between the mass and concentration parameters, such an assumption of a low concentration will lead to an overestimated high mass.

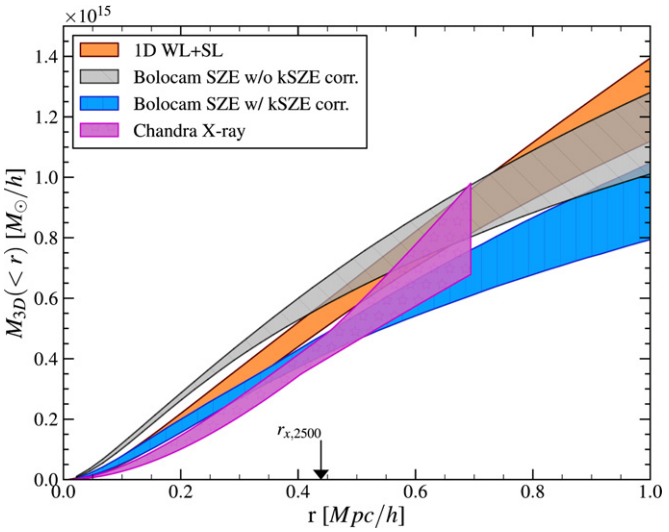

Figure 15. Integrated total mass profiles $M_{\rm 3D}(<r)$, derived from an NFW fit to WL+SL mass reconstruction (orange), from the SZE data after subtracting the best-fit kinetic SZE template found by Mroczkowski et al. (2012) (blue), and from X-ray (magenta). The SZE and X-ray fits are largely consistent with each other, but systematically lower than the lensing derived mass profile at all radii, presumably due to biases associated with the HSE assumption used in deriving both the SZE and X-ray mass profiles. For completeness, we also show the mass profile derived from the SZE data without correcting for the kinetic SZE signal (gray).

(A color version of this figure is available in the online journal.)

We are now in the position to address the probability of finding such a massive cluster in our universe via extreme value statistics (Mortonson et al. 2011; Colombi et al. 2011; Waizmann et al. 2012a; Hotchkiss 2011; Harrison & Coles 2012). In the work of Waizmann et al. (2012a), several high-mass clusters were examined (A2163, A370, RXJ 1347−1145 and 1E0657−558), and the cumulative probability function of finding such massive systems in their given survey area was calculated using general extreme value statistics. However, they found that none of those clusters alone is in tension with ΛCDM. In another paper, Waizmann et al. (2012b) test the probability of the extremely large Einstein radius measured for MACSJ0717, previously estimated as $\theta_E = 55''$ (for $z = 2.5$, Zitrin et al. 2009a) within the standard ΛCDM cosmology. Although they find this system not to be in tension with the ΛCDM expectations, the sensitivity of the Einstein radius distribution to various effects (lens triaxiality, mass–concentration, inner slope of the halo density profile, and more) implies that this comparison is much less reliable than that using a total lensing mass. To conclude, Waizmann et al. (2012b) calculate that a galaxy cluster in the redshift range $0.5 \leqslant z \leqslant 1.0$ would need to have a total mass of at least $M_{200m} = 4.5 \times 10^{15}\,M_\odot$, where M_{200m} is defined with respect to the mean density of the universe at the time of collapse, in order to exclude ΛCDM at the 3σ level.

To compare with Waizmann et al.'s values, MACSJ0717 has $M_{200m} \approx (2.9 \pm 0.5) \times 10^{15}\,M_\odot$ from lensing. In Figure 16, we show the probability distribution function (PDF) of the most massive cluster (for details of this calculation see Davis et al. 2011; Waizmann et al. 2011, 2012a) as calculated for the MACS survey area, $A_S = 22,735\,{\rm deg}^2$, within the a priori redshift interval $0.5 \leqslant z \leqslant 1.0$. We overlay the total mass estimate of

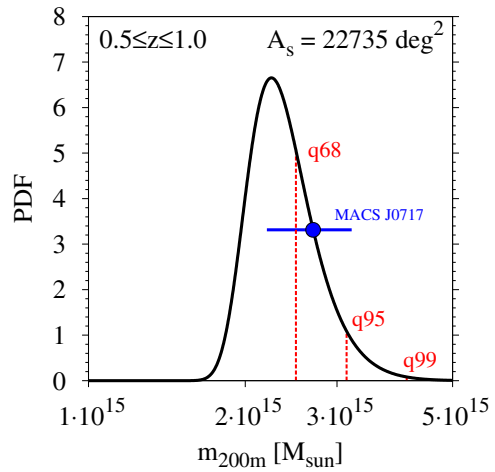

Figure 16. PDF of the maximum cluster mass expected to be found in a survey with sky coverage of the MACS survey, $A_S = 22{,}735\,\mathrm{deg}^2$, within the redshift interval $0.5 \leqslant z \leqslant 1.0$. The red vertical lines represent the 1σ, 2σ, 3σ upper confidence levels. The blue circle denotes the measured lensing mass of MACSJ0717.

(A color version of this figure is available in the online journal.)

MACSJ0717 as the blue error bar. It can be seen that the mass of MACSJ0717 falls slightly below the 95 percent quantile. In order to avoid the bias in the occurrence probabilities of rare galaxy clusters as discussed in Hotchkiss (2011), one has to set the redshift interval a priori. Since MACSJ0717 happens to fall at the lower end of the chosen redshift interval, the PDF in Figure 16 can be considered as a conservative estimate of the true rareness of the cluster such that a more thorough treatment, as presented in Harrison & Hotchkiss (2013), would yield a lower rareness.

Therefore, we conclude that MACSJ0717's mass, being the largest above $z = 0.5$, does not pose any tension on the standard ΛCDM cosmology. However, the growing number of very massive clusters at high redshifts makes it advisable to study the occurrence probabilities of ensembles of massive clusters instead of single ones (see, e.g., Waizmann et al. 2013).

10. SUMMARY AND CONCLUSIONS

In this paper, we have presented a comprehensive lensing analysis of the merging cluster MACSJ0717 at $z = 0.5458$, the largest known cosmic lens with complex internal structures, by combining independent constraints from WL distortion, magnification, and SL effects. This is based on wide-field Subaru+CFHT $u^* B V R_c i' z' J K_S$ imaging, combined with detailed deep CLASH-*HST* 16-band imaging in the cluster core.

We have obtained an improved SL reanalysis of the inner mass distribution from the CLASH *HST* data and confirmed our earlier model (Zitrin et al. 2009a), where we now measure the effective Einstein radius of $60 \pm 6''$ ($z = 2.963$) in agreement with previous values.

The deep Subaru multi-band photometry is used to separate background, foreground, and cluster galaxy populations using the multi-color selection techniques established in our earlier work (Medezinski et al. 2010; Umetsu et al. 2010), allowing us to obtain a reliable WL signal free from significant contamination of unlensed cluster and foreground galaxies for this relatively high redshift cluster. By combining complementary SL, WL distortion, and magnification measurements, we have constructed a model-free mass distribution out to well beyond the virial radius ($r_{\rm vir} \approx 2$ Mpc h^{-1}), effectively breaking the mass-sheet degeneracy.

By fitting projected NFW profiles to the reconstructed mass profiles, we obtain consistent virial mass estimates: $M_{\rm vir} = (2.13 \pm 0.47) \times 10^{15}\, M_\odot\, h^{-1}$ from the joint likelihood analysis of tangential shear, magnification, and SL measurements and $M_{\rm vir} = (2.23 \pm 0.41) \times 10^{15}\, M_\odot\, h^{-1}$ from the joint likelihood analysis of 2D shear and azimuthally averaged magnification measurements.

We further performed a 2D lensing analysis to compare the reconstructed total mass distribution with the luminosity and galaxy distributions over a wide Subaru FOV. The Subaru data reveal the presence of several mass components that lie along a filamentary structure at the cluster redshift. We modeled the 2D shear field with a composite of nine NFW halos in projection, corresponding to mass peaks detected above 2.5σ, including the main cluster approximated by an eNFW halo. Those mass halos, which are part of the $z \approx 0.55$ structure, seem to form a filamentary-like structure that spans 4 Mpc h^{-1}. The sum of the two halos that lie within the virial radius, $M_{\rm vir}(z_5 + z_6) \approx (1.96 \pm 0.28) \times 10^{15}\, M_\odot\, h^{-1}$, is in good agreement with the total mass estimates from the single-NFW fits to the two joint likelihood analyses we have performed. We conclude that the four mass halos, which are confined to the volume within $\approx 2 r_{\rm vir}$, i.e., the turn-over radius, will likely accrete onto the main cluster to form an even more massive system by $z = 0$, as much as $M_{\rm vir} \approx 2.5 \times 10^{15}\, M_\odot\, h^{-1}$ ($\simeq 3.6 \times 10^{15}\, M_\odot$).

Utilizing the high-resolution *HST*-CLASH observations, we were able to resolve the inner core region of the cluster using two independent non-parametric methods, one relying on the WL and one combining both WL+SL constraints. Both show a good overall agreement between the light and the total mass distribution. However, the current spatial resolution is not enough to precisely measure the offsets (if any) between DM, galaxy, and X-ray centroids. The upcoming "Frontier Fields" initiative with *HST* will target six massive lensing clusters, MACSJ0717 among them, and will yield unparalleled deep and detailed mass maps of this complicated merging cluster, which will allow for the first time to significantly determine the possible offsets between the mass components of MACSJ0717, and improve current constraints on the collisional nature of DM.

Using extreme value statistics, we found that our mean mass estimate of $M_{\rm vir} \approx 2 \times 10^{15}\, M_\odot\, h^{-1}$ does not lie outside ΛCDM predictions, for which a higher mass of at least $M_{\rm vir} \approx 3.5 \times 10^{15}\, M_\odot\, h^{-1}$ is required for ΛCDM to be ruled out at the 3σ level, but instead differs only at the 2σ level, so that larger samples of clusters are motivated by our findings to provide a more definitive joint probability.

In conclusion, we find MACSJ0717 to be the most massive cluster so far detected at $z > 0.5$, and to exhibit significant substructure not only in the center, but also to be part of a LSS that spans over ~ 4 Mpc h^{-1}, accreting nearby clusters themselves as massive as few $\times 10^{14}\, M_\odot\, h^{-1}$. This prominence of surrounding structure that we find in our work, including subclusters and filaments together with the ongoing merging activity found in the core of MACSJ0717, indicate that this object is relatively unevolved compared to massive clusters at lower redshift where relaxed clusters such as A1689 show little surrounding structures.

We acknowledge useful discussions with Nobuhiro Okabe, Assaf Horesh, Omer Bromberg, and Preethi Nair. We thank Nick

Kaiser for making the IMCAT package publicly available. We thank G. Mark Voit for having contributed to the ACCEPT-based X-ray mass measurements in advance of publication. We are grateful to Zoltan Levay who crafted the *HST* color image. We are grateful to Jason Rhodes and Richard Massey for providing us with the RRG package.

The CLASH Multi-Cycle Treasury Program is based on observations made with the NASA/ESA *Hubble Space Telescope*. The Space Telescope Science Institute is operated by the Association of Universities for Research in Astronomy, Inc. under NASA contract NAS 5-26555. ACS was developed under NASA contract NAS 5-32864. E.M. is supported by NASA grant HST-GO-12065.01-A. K.U. acknowledges partial support from the National Science Council of Taiwan (grant NSC100-2112-M-001-008-MY3) and from the Academia Sinica Career Development Award. The Bolocam observations were partially supported by the Gordon and Betty Moore Foundation. This material is based upon work at the Caltech Submillimeter Observatory, which is operated by the California Institute of Technology under cooperative agreement with the National Science Foundation (AST-0838261). J.S. is supported by NSF/AST0838261 and NASA/NNX11AB07G. N.C. is partially supported by a NASA Graduate Student Research Fellowship. A.Z. is supported by the "Internationale Spitzenforschung II/2" of the Baden-Württemberg Stiftung. T.M. is provided by NASA through the Einstein Fellowship Program, grant PF0-110077. This research was carried out in part at the Jet Propulsion Laboratory, California Institute of Technology, under a contract with NASA. M.N. acknowledges support from PRIN-INAF 2010.

REFERENCES

Allen, S. W., Schmidt, R. W., Ebeling, H., Fabian, A. C., & van Speybroeck, L. 2004, MNRAS, 353, 457
Arnaud, M., Pratt, G. W., Piffaretti, R., et al. 2010, A&A, 517, A92 (20 pages)
Bahcall, N. A., Lubin, L. M., & Dorman, V. 1995, ApJL, 447, L81
Bartelmann, M., & Schneider, P. 2001, PhR, 340, 291
Beers, T. C., Flynn, K., & Gebhardt, K. 1990, AJ, 100, 32
Benítez, N. 2000, ApJ, 536, 571
Benítez, N., Ford, H., Bouwens, R., et al. 2004, ApJS, 150, 1
Bertin, E. 2006, in ASP Conf. Ser. 351, Astronomical Data Analysis Software and Systems XV, ed. C. Gabriel, C. Arviset, D. Ponz, & S. Enrique (San Francisco, CA: ASP), 112
Bertin, E., & Arnouts, S. 1996, A&AS, 117, 393
Bertin, E., Mellier, Y., Radovich, M., et al. 2002, in ASP Conf. Ser. 281, Astronomical Data Analysis Software and Systems XI, ed. D. A. Bohlender, D. Durand, & T. H. Handley (San Francisco, CA: ASP), 228
Bhattacharya, S., Heitmann, K., White, M., et al. 2011, ApJ, 732, 122
Bonafede, A., Brüggen, M., van Weeren, R., et al. 2012, MNRAS, 426, 40
Bonafede, A., Feretti, L., Giovannini, G., et al. 2009, A&A, 503, 707
Bond, J. R., Kofman, L., & Pogosyan, D. 1996, Natur, 380, 603
Broadhurst, T., Benítez, N., Coe, D., et al. 2005a, ApJ, 621, 53
Broadhurst, T., Takada, M., Umetsu, K., et al. 2005b, ApJL, 619, L143
Broadhurst, T., Umetsu, K., Medezinski, E., Oguri, M., & Rephaeli, Y. 2008, ApJL, 685, L9
Bryan, G. L., & Norman, M. L. 1998, ApJ, 495, 80
Burns, J. O., Hallman, E. J., Gantner, B., Motl, P. M., & Norman, M. L. 2008, ApJ, 675, 1125
Cavagnolo, K. W., Donahue, M., Voit, G. M., & Sun, M. 2008, ApJ, 682, 821
Chongchitnan, S., & Silk, J. 2012, PhRvD, 85, 063508
Clowe, D., Bradač, M., Gonzalez, A. H., et al. 2006, ApJL, 648, L109
Clowe, D., Gonzalez, A., & Markevitch, M. 2004, ApJ, 604, 596
Coe, D., Benítez, N., Broadhurst, T., & Moustakas, L. A. 2010, ApJ, 723, 1678
Coe, D., Benítez, N., Sánchez, S. F., et al. 2006, AJ, 132, 926
Coe, D., Umetsu, K., Zitrin, A., et al. 2012, ApJ, 757, 22
Colless, M., Dalton, G., Maddox, S., et al. 2001, MNRAS, 328, 1039
Colombi, S., Davis, O., Devriendt, J., Prunet, S., & Silk, J. 2011, MNRAS, 414, 2436
Davis, O., Devriendt, J., Colombi, S., Silk, J., & Pichon, C. 2011, MNRAS, 413, 2087
Duffy, A. R., Schaye, J., Kay, S. T., & Dalla Vecchia, C. 2008, MNRAS, 390, L64
Ebeling, H., Barrett, E., & Donovan, D. 2004, ApJL, 609, L49
Ebeling, H., Barrett, E., Donovan, D., et al. 2007, ApJL, 661, L33
Ebeling, H., Edge, A. C., Allen, S. W., et al. 2000, MNRAS, 318, 333
Ebeling, H., Edge, A. C., & Henry, J. P. 2001, ApJ, 553, 668
Ebeling, H., Edge, A. C., Mantz, A., et al. 2010, MNRAS, 407, 83
Edge, A. C., Ebeling, H., Bremer, M., et al. 2003, MNRAS, 339, 913
Fioc, M., & Rocca-Volmerange, B. 1997, A&A, 326, 950
Foley, R. J., Andersson, K., Bazin, G., et al. 2011, ApJ, 731, 86
Green, J., Schechter, P., Baltay, C., et al. 2012, arXiv:1208.4012
Harrison, I., & Coles, P. 2012, MNRAS, 421, L19
Harrison, I., & Hotchkiss, S. 2013, JCAP, 07, 022
Heymans, C., Van Waerbeke, L., Bacon, D., et al. 2006, MNRAS, 368, 1323
Hoekstra, H., Mahdavi, A., Babul, A., & Bildfell, C. 2012, MNRAS, 427, 1298
Hotchkiss, S. 2011, JCAP, 07, 004
Hoyle, B., Jimenez, R., & Verde, L. 2011, PhRvD, 83, 103502
Huchra, J., Jarrett, T., Skrutskie, M., et al. 2005, in ASP Conf. Ser. 329, Nearby Large-Scale Structures and the Zone of Avoidance, ed. A. P. Fairall & P. A. Woudt (San Francisco, CA: ASP), 135
Ilbert, O., Capak, P., Salvato, M., et al. 2009, ApJ, 690, 1236
Ivezic, Z., Tyson, J. A., Allsman, R., et al. 2008, arXiv:0805.2366
Jauzac, M., Jullo, E., Kneib, J.-P., et al. 2012, MNRAS, 426, 3369
Jee, M. J., Rosati, P., Ford, H. C., et al. 2009, ApJ, 704, 672
Jee, M. J., White, R. L., Benítez, N., et al. 2005, ApJ, 618, 46
Kaiser, N., Squires, G., & Broadhurst, T. 1995, ApJ, 449, 460
Katgert, P., Biviano, A., & Mazure, A. 2004, ApJ, 600, 657
Kitayama, T., & Suto, Y. 1996, ApJ, 469, 480
Koekemoer, A. M., Faber, S. M., Ferguson, H. C., et al. 2011, ApJS, 197, 36
Komatsu, E., Dunkley, J., Nolta, M. R., et al. 2009, ApJS, 180, 330
Korngut, P. M., Dicker, S. R., Reese, E. D., et al. 2011, ApJ, 734, 10
Laureijs, R., Amiaux, J., Arduini, S., et al. 2011, arXiv:1110.3193
Lee, J., & Komatsu, E. 2010, ApJ, 718, 60
Limousin, M., Ebeling, H., Richard, J., et al. 2012, A&A, 544, A71
Ma, C.-J., Ebeling, H., & Barrett, E. 2009, ApJL, 693, L56
Ma, C.-J., Ebeling, H., Donovan, D., & Barrett, E. 2008, ApJ, 684, 160
Macario, G., Markevitch, M., Giacintucci, S., et al. 2011, ApJ, 728, 82
Mahdavi, A., Hoekstra, H., Babul, A., et al. 2007, ApJ, 664, 162
Mantz, A., Allen, S. W., Ebeling, H., & Rapetti, D. 2008, MNRAS, 387, 1179
Mantz, A., Allen, S. W., Ebeling, H., Rapetti, D., & Drlica-Wagner, A. 2010a, MNRAS, 406, 1773
Mantz, A., Allen, S. W., Rapetti, D., & Ebeling, H. 2010b, MNRAS, 406, 1759
Markevitch, M., Gonzalez, A. H., David, L., et al. 2002, ApJL, 567, L27
Markevitch, M., Govoni, F., Brunetti, G., & Jerius, D. 2005, ApJ, 627, 733
Marriage, T. A., Acquaviva, V., Ade, P. A. R., et al. 2011, ApJ, 737, 61
Massey, R., Heymans, C., Bergé, J., et al. 2007a, MNRAS, 376, 13
Massey, R., Rhodes, J., Ellis, R., et al. 2007b, Natur, 445, 286
Mastropietro, C., & Burkert, A. 2008, MNRAS, 389, 967
Medezinski, E., Broadhurst, T., Umetsu, K., Benítez, N., & Taylor, A. 2011, MNRAS, 414, 1840
Medezinski, E., Broadhurst, T., Umetsu, K., et al. 2007, ApJ, 663, 717
Medezinski, E., Broadhurst, T., Umetsu, K., et al. 2010, MNRAS, 405, 257
Melchior, P., Viola, M., Schäfer, B. M., & Bartelmann, M. 2011, MNRAS, 412, 1552
Menanteau, F., Hughes, J. P., Sifón, C., et al. 2012, ApJ, 748, 7
Meneghetti, M., Fedeli, C., Zitrin, A., et al. 2011, A&A, 530, A17
Meneghetti, M., Rasia, E., Merten, J., et al. 2010, A&A, 514, A93
Merten, J., Cacciato, M., Meneghetti, M., Mignone, C., & Bartelmann, M. 2009, A&A, 500, 681
Merten, J., Coe, D., Dupke, R., et al. 2011, MNRAS, 417, 333
Miyazaki, S., Komiyama, Y., Sekiguchi, M., et al. 2002, PASJ, 54, 833
Molnar, S. M., Hearn, N. C., & Stadel, J. G. 2012, ApJ, 748, 45
Mortonson, M. J., Hu, W., & Huterer, D. 2011, PhRvD, 83, 023015
Mroczkowski, T. 2011, ApJL, 728, L35
Mroczkowski, T., Dicker, S., Sayers, J., et al. 2012, ApJ, 761, 47
Nagai, D., Vikhlinin, A., & Kravtsov, A. V. 2007, ApJ, 655, 98
Navarro, J. F., Frenk, C. S., & White, S. D. M. 1996, ApJ, 462, 563
Neto, A. F., Gao, L., Bett, P., et al. 2007, MNRAS, 381, 1450
Nonino, M., Dickinson, M., Rosati, P., et al. 2009, ApJS, 183, 244
Oguri, M., Bayliss, M. B., Dahle, H., et al. 2012, MNRAS, 420, 3213
Oguri, M., & Blandford, R. D. 2009, MNRAS, 392, 930
Oguri, M., & Hamana, T. 2011, MNRAS, 414, 1851
Oguri, M., Takada, M., Okabe, N., & Smith, G. P. 2010, MNRAS, 405, 2215
Okabe, N., Bourdin, H., Mazzotta, P., & Maurogordato, S. 2011, ApJ, 741, 116
Okabe, N., & Umetsu, K. 2008, PASJ, 60, 345

Ouchi, M., Shimasaku, K., Okamura, S., et al. 2004, ApJ, 611, 660
Owers, M. S., Randall, S. W., Nulsen, P. E. J., et al. 2011, ApJ, 728, 27
Planck Collaboration, Ade, P. A. R., Aghanim, N., et al. 2011, A&A, 536, A8
Postman, M., Coe, D., Benítez, N., et al. 2012, ApJS, 199, 25
Rapetti, D., Allen, S. W., Mantz, A., & Ebeling, H. 2010, MNRAS, 406, 1796
Rasia, E., Meneghetti, M., Martino, R., et al. 2012, NJPh, 14, 055018
Rasia, E., Tormen, G., & Moscardini, L. 2004, MNRAS, 351, 237
Rhodes, J., Refregier, A., & Groth, E. J. 2000, ApJ, 536, 79
Ricker, P. M., & Sarazin, C. L. 2001, ApJ, 561, 621
Rines, K., Geller, M. J., Diaferio, A., Kurtz, M. J., & Jarrett, T. H. 2004, AJ, 128, 1078
Rines, K., Geller, M. J., Diaferio, A., Mohr, J. J., & Wegner, G. A. 2000, AJ, 120, 2338
Rosati, P., Tozzi, P., Gobat, R., et al. 2009, A&A, 508, 583
Russell, H. R., Sanders, J. S., Fabian, A. C., et al. 2010, MNRAS, 406, 1721
Santos, J. S., Fassbender, R., Nastasi, A., et al. 2011, A&A, 531, L15
Sayers, J., Czakon, N. G., Mantz, A., et al. 2013, ApJ, 768, 177
Sayers, J., Golwala, S. R., Ameglio, S., & Pierpaoli, E. 2011, ApJ, 728, 39
Schlegel, D. J., Bebek, C., Heetderks, H., et al. 2009, arXiv:0904.0468
Schmidt, R. W., & Allen, S. W. 2007, MNRAS, 379, 209
Springel, V., & Farrar, G. R. 2007, MNRAS, 380, 911
Takada, M. 2010, in AIP Conf. Ser. 1279, Deciphering the Ancient Universe with Gamma-Ray Bursts, ed. N. Kawai & S. Nagataki (Melville, NY: AIP), 120
Tegmark, M., Blanton, M. R., Strauss, M. A., et al. 2004, ApJ, 606, 702
Thompson, R., & Nagamine, K. 2012, MNRAS, 419, 3560
Tozzi, P., Santos, J. S., Nonino, M., et al. 2013, A&A, 551, A45
Umetsu, K. 2013, ApJ, 769, 13
Umetsu, K., Birkinshaw, M., Liu, G.-C., et al. 2009, ApJ, 694, 1643
Umetsu, K., & Broadhurst, T. 2008, ApJ, 684, 177
Umetsu, K., Broadhurst, T., Zitrin, A., Medezinski, E., & Hsu, L. 2011a, ApJ, 729, 127
Umetsu, K., Broadhurst, T., Zitrin, A., et al. 2011b, ApJ, 738, 41
Umetsu, K., Medezinski, E., Broadhurst, T., et al. 2010, ApJ, 714, 1470
Umetsu, K., Medezinski, E., Nonino, M., et al. 2012, ApJ, 755, 56
Umetsu, K., Takada, M., & Broadhurst, T. 2007, MPLA, 22, 2099
Umetsu, K., Tanaka, M., Kodama, T., et al. 2005, PASJ, 57, 877
Vanderlinde, K., Crawford, T. M., de Haan, T., et al. 2010, ApJ, 722, 1180
Van Waerbeke, L., Benjamin, J., Erben, T., et al. 2013, MNRAS, 433, 3373
van Weeren, R. J., Röttgering, H. J. A., Brüggen, M., & Cohen, A. 2009, A&A, 505, 991
van Weeren, R. J., Röttgering, H. J. A., Intema, H. T., et al. 2012, A&A, 546, A124
Vikhlinin, A., Burenin, R. A., Ebeling, H., et al. 2009a, ApJ, 692, 1033
Vikhlinin, A., Kravtsov, A., Forman, W., et al. 2006, ApJ, 640, 691
Vikhlinin, A., Kravtsov, A. V., Burenin, R. A., et al. 2009b, ApJ, 692, 1060
von der Linden, A., Allen, M. T., Applegate, D. E., et al. 2012, arXiv:1208.0597
Waizmann, J.-C., Ettori, S., & Bartelmann, M. 2013, MNRAS, 432, 914
Waizmann, J.-C., Ettori, S., & Moscardini, L. 2011, MNRAS, 418, 456
Waizmann, J.-C., Ettori, S., & Moscardini, L. 2012a, MNRAS, 420, 1754
Waizmann, J.-C., Redlich, M., & Bartelmann, M. 2012b, A&A, 547, A67
Watanabe, E., Takizawa, M., Nakazawa, K., et al. 2011, PASJ, 63, 357
White, M., Blanton, M., Bolton, A., et al. 2011, ApJ, 728, 126
Wuyts, S., Labbé, I., Schreiber, N. M. F., et al. 2008, ApJ, 682, 985
Yagi, M., Kashikawa, N., Sekiguchi, M., et al. 2002, AJ, 123, 66
Zhao, D. H., Jing, Y. P., Mo, H. J., & Börner, G. 2009, ApJ, 707, 354
Zitrin, A., Broadhurst, T., Coe, D., et al. 2011, ApJ, 742, 117
Zitrin, A., Broadhurst, T., Rephaeli, Y., & Sadeh, S. 2009a, ApJL, 707, L102
Zitrin, A., Broadhurst, T., Umetsu, K., et al. 2009b, MNRAS, 396, 1985
Zitrin, A., Meneghetti, M., Umetsu, K., et al. 2013, ApJL, 762, L30
Zitrin, A., Rephaeli, Y., Sadeh, S., et al. 2012a, MNRAS, 420, 1621
Zitrin, A., Rosati, P., Nonino, M., et al. 2012b, ApJ, 749, 97